Neuroinformatics (2022) 20:1013–1039
https://doi.org/10.1007/s12021-022-09576-5

ORIGINAL ARTICLE

Cortical Representation of Touch in Silico

Chao Huang[1] · **Fleur Zeldenrust**[2] · **Tansu Celikel**[2,3]

Accepted: 19 February 2022 / Published online: 29 April 2022

Abstract
With its six layers and ~ 12,000 neurons, a cortical column is a complex network whose function is plausibly greater than the sum of its constituents'. Functional characterization of its network components will require going beyond the brute-force modulation of the neural activity of a small group of neurons. Here we introduce an open-source, biologically inspired, computationally efficient network model of the somatosensory cortex's granular and supragranular layers after reconstructing the barrel cortex in soma resolution. Comparisons of the network activity to empirical observations showed that the in silico network replicates the known properties of touch representations and whisker deprivation-induced changes in synaptic strength induced in vivo. Simulations show that the history of the membrane potential acts as a spatial filter that determines the presynaptic population of neurons contributing to a post-synaptic action potential; this spatial filtering might be critical for synaptic integration of top-down and bottom-up information.

Keywords Somatosensory (barrel) cortex · Large-scale biophysical simulations · Touch representation · Plasticity · Adaptation

Introduction

One of the grand challenges in neuroscience is to mechanistically describe the cerebral cortical function. Numerous studies have identified the organizational principles of cortical circuits in various cortical areas across model systems by describing the principles of neuronal classification, cell-type specific projection patterns, input–output mapping across cortical layers, and by functional characterization of the anatomically identified neurons upon simple stimulation conditions, (see e.g. Douglas & Martin, 2004; Markram et al., 2015). Although a wiring-diagram approach is critical for a *structural* description of the network, relating the anatomical structure to network *function* will require a detailed study of the dynamical processes in single neurons as well as neural populations (Douglas & Martin, 2007; O'Connor et al., 2009). Or, in other words, one of the best ways to understand the functioning of the brain is trying to build one (Einevoll et al., 2019; Eliasmith & Trujillo, 2014). Accordingly, a large number of large-scale reconstructed computational models of cortical function (see Supplemental Table 1 for a direct comparison of the most recent models; also see the discussion section and this recent review (Fan & Markram, 2019)), including macaque (Chariker et al., 2016; Schmidt et al., 2018a, b; Schuecker et al., 2017; Zhu et al., 2009), cat (Ananthanarayanan et al., 2009) and mouse/rat (Arkhipov et al., 2018; Billeh et al., 2019) visual cortex, rat auditory cortex (Traub et al., 2005), rat hindlimb sensory cortex (Markram et al., 2015), cerebellum (Sudhakar et al., 2017) and "stereotypical" mammalian neocortex (Izhikevich & Edelman, 2008; Markram, 2006; Potjans & Diesmann, 2014; Reimann et al., 2013; Tomsett et al., 2015), have been introduced, where neuronal dynamics are approximated using neuron models that range from integrate-and-fire point neurons (Ananthanarayanan et al., 2009; Bernardi et al., 2021; Chariker et al., 2016; Landau et al., 2016; Potjans & Diesmann, 2014; Schmidt et al., 2018a, b; Schuecker et al., 2017; Sharp et al., 2014; Zhu et al., 2009) to morphologically reconstructed multi-compartment neurons (Arkhipov et al., 2018; Billeh et al., 2019; Izhikevich

Chao Huang and Fleur Zeldenrust denotes equal contribution.

✉ Tansu Celikel
celikel@gatech.edu

[1] Department of Biology, University of Leipzig, Leipzig, Germany

[2] Donders Institute for Brain, Cognition, and Behaviour, Radboud University, Nijmegen, the Netherlands

[3] School of Psychology, Georgia Institute of Technology, Atlanta, GA, USA

& Edelman, 2008; Markram, 2006; Markram et al., 2015; Reimann et al., 2013; Sudhakar et al., 2017; Tomsett et al., 2015; Traub et al., 2005). These models have given insights in a range of topics including the nature of the local field potentials (Reimann et al., 2013; Tomsett et al., 2015), mechanisms of state transitions (Markram et al., 2015), frequency selectivity (Zhu et al., 2009), the influence of single-neuron properties on network activity (Arkhipov et al., 2018) and the relation between connectivity patterns and single-cell functional properties (i.e. receptive fields, (Billeh et al., 2019)).

With its topographical organization, well-characterized structural and functional organization, and its ever growing number of publicly available molecular, cellular and behavioural big datasets (Azarfar et al., 2018b; da Silva Lantyer et al., 2018; Kole et al., 2017; Kole, Lindeboom et al., 2018; Kole, Scheenen et al., 2018), the barrel column is ideally suited as a model system for computational reconstruction of circuit organization and function. Accordingly, large-scale computational models of the rodent barrel cortex, ranging from detailed reconstructed models that need to be run on a supercomputer (Phoka et al., 2012; Sharp et al., 2014) to much less detailed and computationally expensive models (Bernardi et al., 2021; Landau et al., 2016), have been developed. Here, we present the results of a reconstruction of the barrel cortical network in soma resolution, using different stainings to mark different types of neurons (anti-NeuN, anti-GABA, anti-Calretenin, anti-Somatostatin, anti-Parvalbumin, anti-vasointestinal peptide). We present the results of this reconstruction as an open-source biologically constrained computational network model of the granular and supragranular layers of the barrel cortex along with the ventroposterior medial thalamus. It is a detailed model, with cortical cell densities based on the reconstructions in soma resolution presented herein and our previous work on a temporal variation in response dynamics (Huang et al., 2016). The code can be run on a desktop computer with or without a CUDA enabled GPU and is available for download on GitHub (https://github.com/DepartmentofNeurophysiology/Cortical-representation-of-touch-in-silico for the Matlab implementation, which is computationally fast; https://github.com/DepartmentofNeurophysiology/Cortical-representation-of-touch-in-silico-NetPyne for NetPyNE, an implementation that allows for easy export to other platforms and flexibility in terms of modalities such as the neuron models). Here we show that this barrel cortex in silico can predict (a) emergent whisker representations, (b) changes in the synaptic strength upon whisker deprivation, (c) network representation of touch from behavioral data, using only the information extracted from whisker tracking. The model will help to unravel novel principles of information processing (Huang et al., 2020).

Results

Anatomical Organization of the Barrel Cortex

Just like most other neocortical areas, barrel columns consist of six layers with distinct molecular fingerprints and tens of different neural classes (Azarfar et al., 2018a, b; Fox, 2018; Kole, Lindeboom et al., 2018; Kole, Scheenen et al., 2018; Markram et al., 2004; Oberlaender et al., 2012; Thomson & Lamy, 2007). The reconstruction of the network in soma resolution (Fig. 1, for detailed methods, see Materials and Methods) shows that the laminar distribution of cell-types varies significantly across layers. Similar to the laminar borders observed in the traditional Nissl staining, staining the column with neuronal nuclear antibody anti-NeuN, hereafter NeuN, results in a higher cellular density in Layer (L)4 and lower layers of L3 in comparison to L2 and L5-6. Inhibitory neurons stained with anti-GABA do not obey the laminar borders as outlined by the NeuN and display near equal densities in lower L4, L5b, and L1. Specific inhibitory neuron markers, however, have distinct expression patterns across the laminae: While Calretinin neurons are predominantly found in the L4/L3 border, Somatostatin neurons are preferentially located in the infragranular layers (Fig. 1E). Parvalbumin-positive interneurons, on the other hand, are found at higher densities in L4 and L5. (Fig. 1E). The cellular distributions in the canonical D-row column can be found in Supplemental Table 2.

Stimulus Representations in Silico Network

To create a network model, three components are necessary: 1) the distribution of the neurons (nodes of the network), 2) the connections between the neurons (edges of the network) and 3) a dynamic model of information transfer in single neurons/nodes. The first of these components, the distribution of neurons, was measured in the previous section (Fig. 1). The second component, network connectivity, was determined using axonal and dendritic projection patterns (Egger et al., 2008; Feldmeyer et al., 2002, 2006; Helmstaedter et al., 2008; Lübke et al., 2003), which were approximated by 3-D Gaussian functions (see Materials and Methods and Supplemental Table 3), with the assumption that the probability that two neurons are connected is proportional to the degree of axonal-dendritic overlap between these two neurons (i.e. Peter's rule, (White, 1979)). So the probability of axon-dendrite overlap and hence connection is a function of distance from the source neuron. For the third component, the dynamic model of single neurons, we modified the computationally efficient Izhikevich neuron model ((Izhikevich, 2003, 2004), see Materials and Methods and

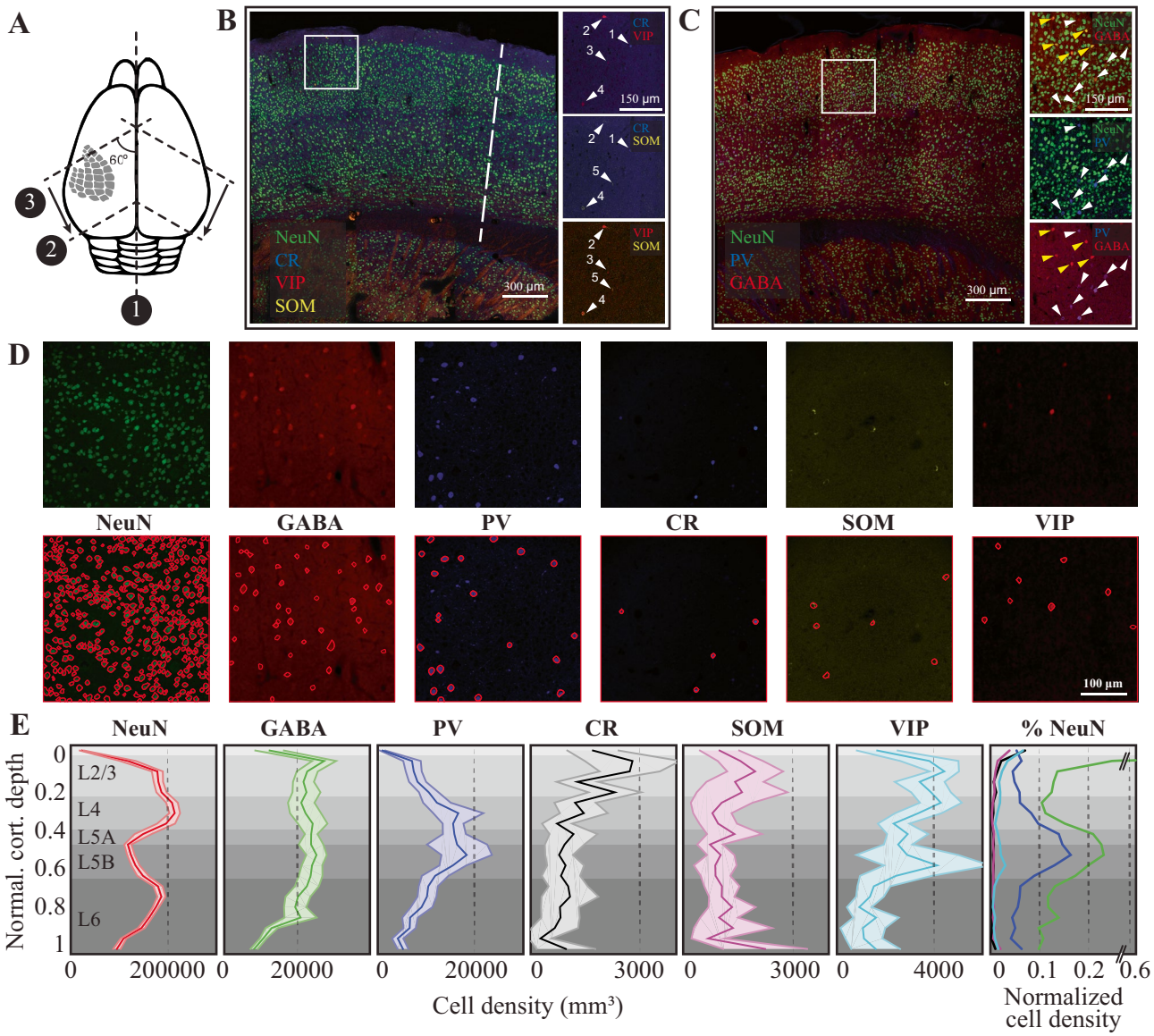

Fig. 1 The anatomy of the canonical cortical column in the mouse barrel cortex. (**A**) Schematic representation of the slicing approach. Numbers refer to the order of incision (1, 2) and sectioning (3) (see Materials and Methods for details). (**B**-**C**) Six monoclonal antibodies raised against select cellular markers were used for co-staining cellular classes. Insets show different staining patterns. Cell labeled with the same number is the same cell across different stainings. (**D**) Randomly selected raw images (top row) along with automatically detected cells in a 300×300x25 microm volume of fixed tissue (see Materials and Methods for details). (**E**) Density of identified cellular populations across the six cortical layers. The shaded regions represent 2 standard deviations from the mean (N = 22 slices for NeuN, 12 for GABA, PV and 10 for CR, SOM, VIP; in average 3 columns in each slice from 3 animals, 5 hemispheres. Values are mean and std calculated from each slice). The last column represents the relative cellular density after normalizing the cell count to the number of NeuN positive neurons in a given layer

Supplemental Table 4) to include the inverse relationship between the first derivative of the membrane potential, i.e. the speed with which the synaptic depolarization rises, and the action potential threshold, so that the threshold is a function of the history of the membrane potential (the membrane state Huang et al., 2016; Zeldenrust et al., 2020)). This modification in the quadratic model did not affect the model's ability to predict the timing of action potentials upon sustained current injection in soma (see Fig. 2A; compare the middle column to (Izhikevich, 2003, 2004) and also correctly predicted the rate and timing changes associated with the membrane state at a single neuron resolution (Fig. 2A).

With the completion of the three required components for functional network creation, we constructed a biologically constrained barrel cortical column in silico. Due to the general lack of experimental data on the pairwise connectivity

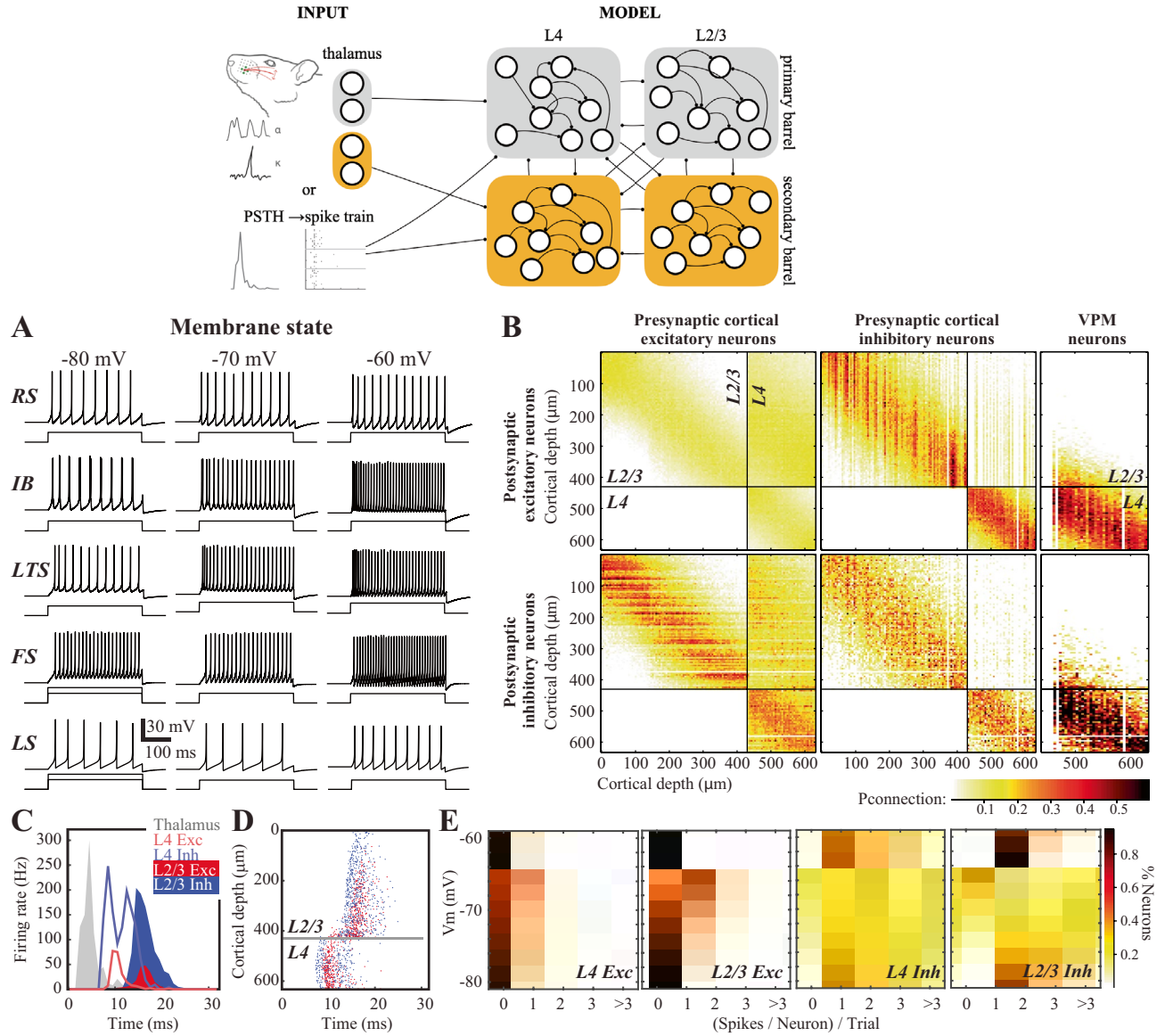

Fig. 2 Neural activity and circuit connectivity in silico. (**A**) Spiking pattern of five electrically characterized cell classes upon somatic step-and-hold current injection across three membrane states. (**B**) The connectivity matrix across the network. (**C**) Emergent cortical activity upon thalamic stimulation, simulated as a response to a single whisker deflection. Peristimulus time histograms (PSTHs) depict population responses across thalamus (see Materials and Methods for details on how the PSTHs from (Petersen et al., 2008) were implemented), and cortical responses. (**D**) Same as in C but action potentials from neurons in the top 630 microm of the cortical column are shown. (**E**) Likelihood of spiking across identified neuron classes and membrane states

between infragranular layer neurons and the rest of the network, in this version of the in silico column, we have constrained the network to the top 630 μm (Fig. 2B), which is border between L4-L5 in the mouse. As the granular layer (L4) is the principal recipient of the thalamic inputs (Azarfar et al., 2018a, b) and strongly drives the supragranular (L1-3) layers, before the cross-columnar integration takes place across the upper L2/3, this model provides an in silico simulation environment for the first three stages of thalamocortical and intracortical information processing that involves supragranular and granular layers.

In the simulated network, stimulus-evoked activity spreads across the network from ventroposterior medial nucleus (VPM) to L2/3 with latencies comparable to those observed in biological networks under anesthesia (Fig. 2C; Allen et al., 2003; Armstrong-James et al., 1992; Celikel et al., 2004). Inhibitory neurons had an earlier onset of spiking with a peak latency of 8.2 ± 0.6 ms (mean ± std) in L4 (Fig. 2C), which corresponds to < 3 ms

conduction delay, calculated from the population peristimulus time histograms (Fig. 2C). These delays are similar to previous observations in vivo (Condylis et al., 2020; Dudai et al., 2020; Sermet et al., 2019; Swadlow, 1995, 2003). In terms of the latency to an action potential, neurons across the entire depth of L4 were homogenous with the exception that those closer to the L3 border showed a delayed spiking (Fig. 2D). As the feed-forward projections originating from L4 are the main inputs to the L2/3 neurons, the activity in silico naturally follows the latency distribution observed in vivo across the cortical layers, with L2 neurons generating action potential up to 4 ms later than the lower L3 neurons (Celikel et al., 2004); Fig. 2C). Independent from the actual location of the neuron within the *silico* network, however, inhibitory neurons have an earlier onset of spiking as compared to the neighboring excitatory neurons within the layer (Fig. 2D), because they receive more and stronger excitatory inputs.

The spiking probability varies significantly across layers and neuron types in vivo (Celikel et al., 2004; De Kock et al., 2007; Gentet et al., 2010, 2012; O'Connor et al., 2010) and in silico (Fig. 2D). Excitatory neurons respond to the stimulus sparsely, as the probability of a given neuron to generate an action potential at a given trial is low. When the stimulus does yield a suprathreshold response, the neuron typically generates a single action potential (Fig. 2E). The response probability and the number of action potentials/stimulus depend on the laminar location of the neuron, its cell type and its subthreshold membrane potential prior to the stimulus (Fig. 2E; (Zeldenrust et al., 2020)). The laminar position of the neuron, be it excitatory or inhibitory, does not play a role in state-dependent changes in excitability at the single neuron level, although neurons in the supragranular layers respond on average more reliably to stimuli. The only exception to this rule is when the stimulus arrives in a hyperpolarized membrane state; if the resting membrane potential prior to the stimulus onset averaged < -75 mV, both excitatory and inhibitory neurons in L2/3 display failure rates higher than corresponding L4 neurons in the same membrane state (Fig. 2E). This is because the thalamus excites mostly L4 and only the bottom of L2/3: since most of the L2/3 neurons receive excitation from L4 and there are less spikes in L4 in hyperpolarized states, there are even less spikes from L2/3 in this state. These increased failure rates suggest that in hyperpolarized states, the activity of the supragranular layer is effectively uncoupled from the bottom-up sensory input.

The Source of Response Variability in Silico

In a network where information propagates across synaptically coupled neurons via relatively weak, failure-prone and sparse connections, identical stimuli in the periphery will evoke distinct neural activation patterns, even if the measured spike rate and time are constant across presynaptic populations (given the stochasticity of the presynaptic population contributing to the postsynaptic spiking) and even if, as in this model, input from ongoing activity in other cortical areas, is not taken into account. Accordingly, neural representations in a biologically inspired *silico* network are expected to vary as a result of both the presynaptic spike timing variability and the changes in *effective connectivity* between layers and across trials discussed in the previous section.

To quantify the extent of the response variability in silico, we simulated the cortical responses to thalamic inputs in two conditions: (1) in every trial each thalamic spike train was generated as a result of an inhomogeneous Poisson process, constrained by the PSTH (see Fig. 3A and Methods section 'Thalamic inputs into the barrel cortex *in silico*'), or (2) a single realization of (1) was repeated over trials, so there was no trial-to-trial variability in the thalamic spike trains (see Fig. 3B) and the thalamic spike trains were identical across trials. While the former condition creates variability in spike timing and the rate at the single thalamic neuron resolution, the latter condition preserves the rate and timing of the thalamic input onto the postsynaptic cortical neurons across trials. The results showed that the effective connectivity, i.e. which presynaptic neurons contribute to the firing of a postsynaptic neuron in a given trial, is a major contributor to the response variability (Fig. 3). This contribution was independent of the membrane state of the postsynaptic neuron and the neuron class, although the variability increased with membrane depolarization (Fig. 3, A2-A3).

Stimulus Representations in L4 in Silico

Thalamic neurons project extensively to cortical L4, and diffusely to the L3/L4 and L5b/6 borders (Arnold et al., 2001; Oberlaender et al., 2012; Sermet et al., 2019). This thalamocortical input is the principal pathway that carries the feedforward excitatory drive, carrying the bottom-up sensory information (Azarfar et al., 2018a, b) L4 representations of the sensory input are characterized by sparse neural representations in vivo (Aguilar & Castro-Alamancos, 2005; Celikel et al., 2004; De Kock et al., 2007) and in silico (Fig. 4). Thalamic input modeling the principal whisker's stimulation in vivo results in a significant firing rate modulation (two orders of magnitude, between 0.02–2.2 spikes/stimulus/cell) in the network, depending on the membrane states of the L4 neurons prior to the stimulus arrival as well as the neuronal class studied (at $vr = -80$ mV, excitatory neurons fire at 0.06 ± 0.11 spikes/stimulus, range 0–0.82; inhibitory neurons, 0.68 ± 0.71

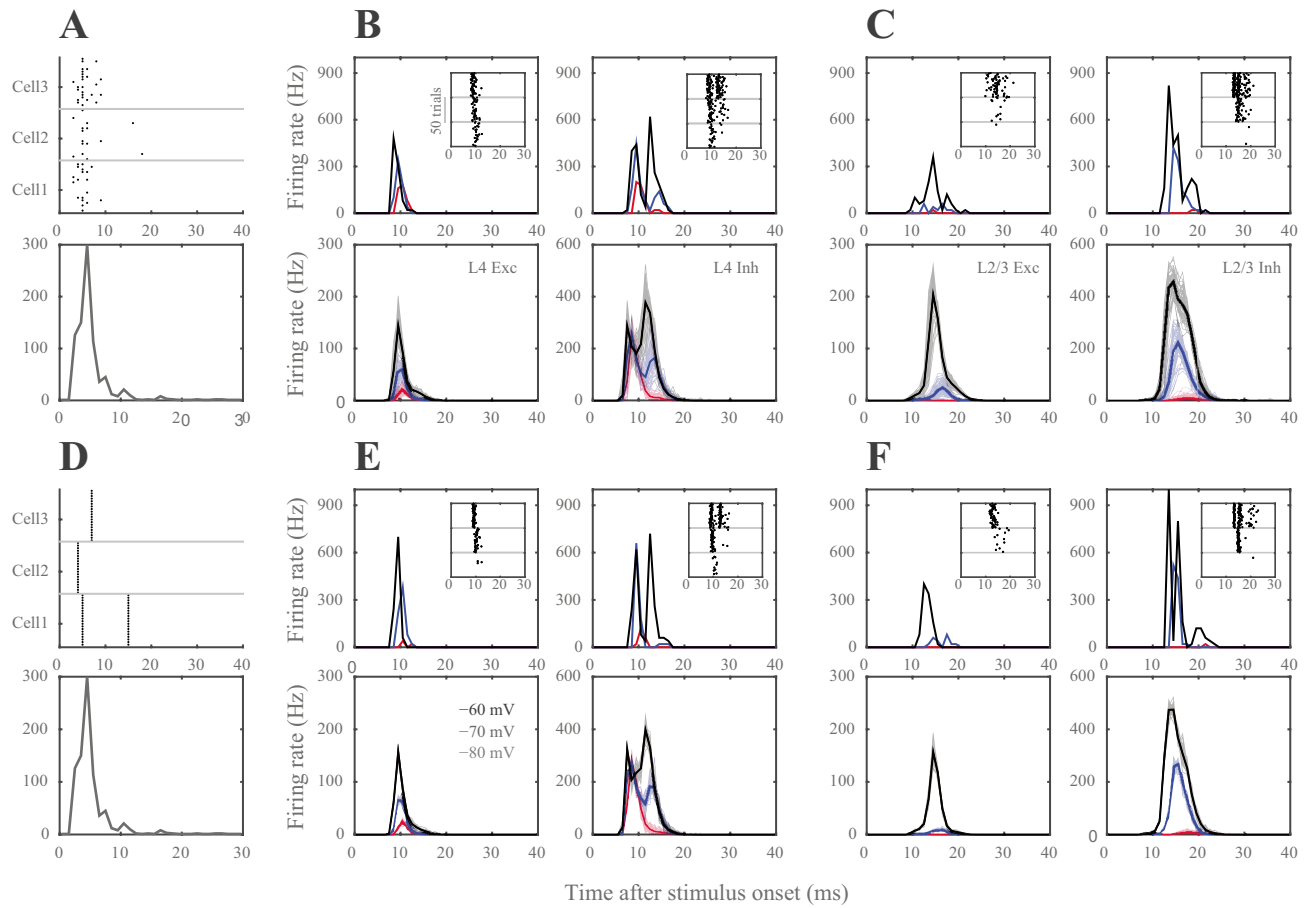

Fig. 3 Variability of stimulus representations in silico. (**A1**) The population activity in thalamus is constrained by the PSTH as spike timing for individual cells are drawn according to Poisson-distributions. Raster plots exemplify the spiking responses of 3 representative thalamic neurons across 20 trials (upper panel, 1 neuron response in different trials) drawn from the population PSTH (lower panel). (**A2**) Representation of the thalamic input in single (upper panels) neurons and populations (lower panels). Left column: L4 excitatory, right column: L4 inhibitory neurons. PSTHs represent neural responses to 50 thalamic stimulation across three different membrane states (black: -60 mV, blue: -70 mV, red: -80 mV) (**A3**) Same as in A2, but for L2/3 excitatory and inhibitory neurons. (**B1**) The population PSTH in thalamus is the same as in A1 (lower panel), but spike timing and rate of individual thalamic neurons' spiking is constant across trials (see raster plots in upper panel). (**B2**, **B3**) same as in A2, A3, but show cortical response to stereotypic thalamic inputs. Note that even when the same thalamic input pattern was used to stimulate the network, neurons still showed spike timing variability due to synaptic failures and synaptic strength variations although the variance was greatly reduced as the effective connectivity in the network was kept constant

spikes/stimulus, range 0–2.22; at $vr = -60$ mV, excitatory neurons, 0.44 ± 0.30 spikes/stimulus, range 0–1.96; inhibitory neurons, 2.13 ± 1.48 spikes/stimulus, range 0.02–6.54; values show mean $\pm$ std). While excitatory neurons fire sparsely, inhibitory neurons spike with higher reliability (Fig. 4C). The resting membrane potential changes the properties of excitatory neurons firing, as L4 excitatory neurons switch from a sparse representation (i.e. the probability of spiking for each neuron per stimulus is low, and when neurons spike they typically fire single action potentials) to less sparse spiking as the membrane potential depolarizes (Fig. 4E). The inhibitory neural population, on the other hand, undergoes rate scaling as the resting membrane potential is depolarized (Fig. 4E).

The spatial distribution of synaptic inputs in a network is primarily constrained by the axo-dendritic overlap across the synaptically connected neurons. Accordingly, with diffuse axonal projections of thalamic neurons, and spatially constrained dendritic branching to the barrel borders, excitatory and inhibitory L4 neurons along the rostro-caudal (RC) and medio-lateral (MC) planes do not display a spatial bias in the tangential plane (Fig. 4B). Unlike this spatial homogeneity of L4 responses to the stimulus, preferential laminar targeting of the thalamic input results in a higher likelihood of spiking in the bottom portion of the barrel, especially for postsynaptic excitatory neurons (Fig. 4F).

The topographical nature of the representation of whisker touch dictates that each neuron has a preferred whisker, called the principal whisker, which evokes the largest number

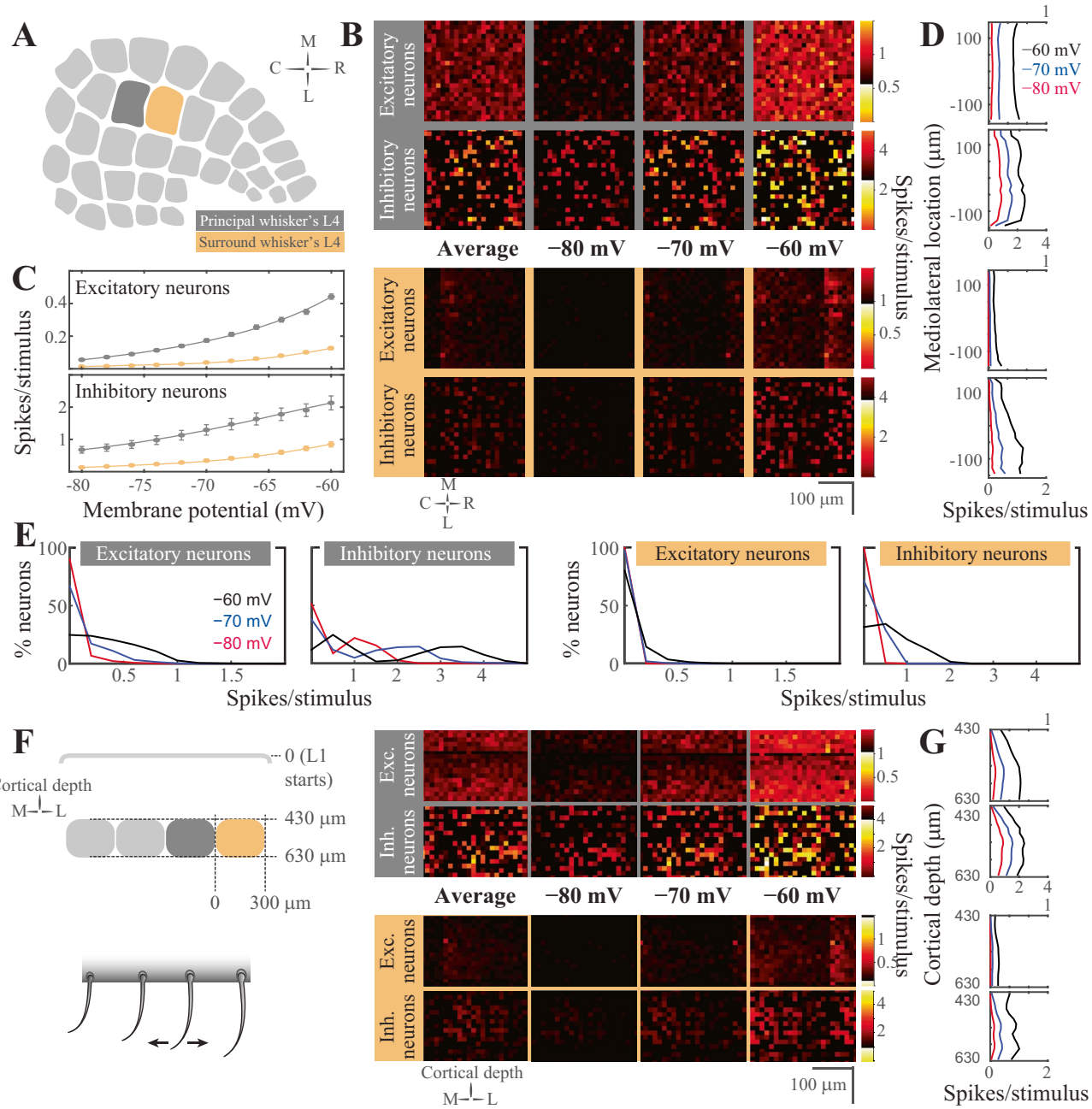

Fig. 4 Stimulus evoked representations in cortical layer 4 in silico. (**A**) Schematic representation of the spatial orientation of the simulated network. The visualizations are in the tangential plane. The principal cortical column is the D2 whisker's column. (**B**) Average neuronal response in rostro-caudal (RC) and medio-lateral (ML) planes, across different resting membrane states (pixel size 15×15 µm in cortical tissue). The figurines on the grey shaded background display the response in the principal whisker's cortical column; the yellow background shows the activity in the first order surrounding L4. (**C**) Average firing rate of excitatory (top) and inhibitory neurons (bottom) in the network as a function of the resting membrane potential before stimulus onset in the principal (top) and surround (bottom) whisker's L4. (**D**) Average firing rate in the ML axis across the membrane states. (**E**) Distribution of the spiking response per stimulus across neuron classes and membrane states. (**F**) Left: Schematic representation of the coronal orientation of the visualized network. Right: Average neuronal response across the dorsoventral plane in L4 (pixel size 15×15 µm in cortical tissue). (**G**) Average firing rate across cortical depth

of action potentials upon deflection (Brecht & Sakmann, 2002; Foeller et al., 2005). However the receptive fields of cortical neurons are rarely (if ever) constrained to a single whisker, as multi-whisker receptive fields in the thalamus (Aguilar & Castro-Alamancos, 2005; Armstrong-James & Callahan, 1991; Diamond et al., 1992; Kwegyir-Afful et al.,

2005; Simons & Carvell, 1989) and cross-columnar projections in the cortex (Egger et al., 2008) ensure that each neuron receives information from multiple whiskers. Responses to the surround whiskers are always weaker, in number of spikes per stimulus, and arrive with a delay compared to the principal whisker deflection (Brecht & Sakmann, 2002). This relationship is preserved in silico representations of touch presented here (Fig. 4B, C, F). Principal *vs* surround whiskers activate excitatory and inhibitory neurons similarly, although evoked representations of surround whiskers are invariably weaker (Fig. 4B). Similar to the principal whisker deflection, surround whisker stimulation results in largely homogenous representations across the RC-ML axis (Fig. 4B) even if the postsynaptic spiking is constrained to depolarized membrane states. The sublaminar activation pattern in L4 results in a higher likelihood of spiking in the bottom half of L4, even after surround whisker stimulation (Fig. 4F).

One main difference between the principal vs surround representations is the role of the membrane state in the modulation of network activity. Unlike the differential role of the resting membrane potential in encoding principal whisker touch across the excitatory and inhibitory networks, the contribution of the different membrane states to surround whisker representation slowly (but predictably) varies across different membrane states (Fig. 4C). Most excitatory and inhibitory neurons in the surround L4 do not represent the stimulus information during the quiescent hyperpolarized membrane state, resulting in principal whisker specific cortical representations. In the depolarized membrane states, the probability of spiking disproportionately increases for the inhibitory neurons.

Stimulus Representations in the Supragranular Layers in Silico

Feedforward L4 projections are powerful modulators of supragranular layers and bring the bottom-up information from the sensory periphery for eventual cross-columnar integration primarily via L2, and less so via upper L3 neurons (Kerr et al., 2007; Petersen, 2007; Petersen & Sakmann, 2001). Principles of sensory representations by L2/3 in silico (Fig. 5) are generally similar to the L4 neurons, with the exceptions that (1) supragranular excitatory neurons have an increased probability of firing during surround whisker stimulation, and (2) the spatial localization of a neuron has predictive power for its response properties.

Unlike the granular layer representations of the stimulus in the quiescent membrane states, L2/3 excitatory neurons are completely silent at hyperpolarized membrane potentials, suggesting that the bottom-up thalamocortical information is decoupled from the rest of the cortical circuits that originate from the supragranular layers. The lack of spiking is not specific to the excitatory neurons, inhibitory neurons are similarly unresponsive to the L4 input if the resting membrane potential was hyperpolarized (Fig. 5C). Although inhibitory neurons fire stimulus-evoked action potentials at hyperpolarized membrane potentials ($<$ -70 mV), the net effect of the membrane potential on suppressing cortical propagation of information via L2 is maintained across both classes of neurons (Fig. 5). The lack of stimulus-evoked spiking in the surround column Fig. 5 in resting membrane potentials $<$ -70 mV and the changes in the spike probability described before suggest that sensory representations are weak but specific to the principal whisker column during the quiescent states in vivo.

Given that the neuronal excitability changes with the membrane state, that the neural thresholds depend on the stimulus and membrane potential history and that each neuron will (not necessarily linearly) sum its inputs until this variable threshold, the effective connectivity within the network should change with the membrane state of the postsynaptic neuron. To visualize the effective connectivity we spatially mapped the presynaptic neurons that fired action potential(s) prior to the spiking of a postsynaptic neuron (Fig. 6), by plotting the postsynaptic spike-triggered presynaptic average (normalized to the average over all pixels and all postsynaptic neurons, so that the relative contribution of each presynaptic neuron is shown). As expected, the effective connectivity varied with the membrane state (note that the the postsynaptic spike-triggered presynaptic average naturally increases with an increase in postsynaptic firing, due to a higher chance of a coincident spikes with higher firing rates). With an increasing probability of L2/3 spiking in the depolarized membrane states, the relative contribution of the intralaminar input to the spiking increased, suggesting that in the depolarized membrane states, sensory representations are a function of feed-forward drive originating from L4 and local changes in excitability in L2/3. The latter component is likely to be modulated by top-down modulations as the state of the animal changes during, for example, active sensing, providing a mechanistic model how the bottom-up sensory information can be integrated with the top-down neuromodulatory influences.

Experience-Dependent Plasticity of Synaptic Strength in Silico

Neurons in the barrel cortex adapt to changes in sensory organ output as cortical circuits undergo plastic changes upon altered sensory input statistics (Allen et al., 2003; Clem et al., 2008; Feldman & Brecht, 2005; Kole, Lindeboom et al., 2018; Kole, Scheenen et al., 2018). These adaptive changes have long-lasting consequences in neural representations of touch. We have, therefore, integrated a spike-timing-dependent plasticity learning rule (Celikel et al., 2004) to enable plastic

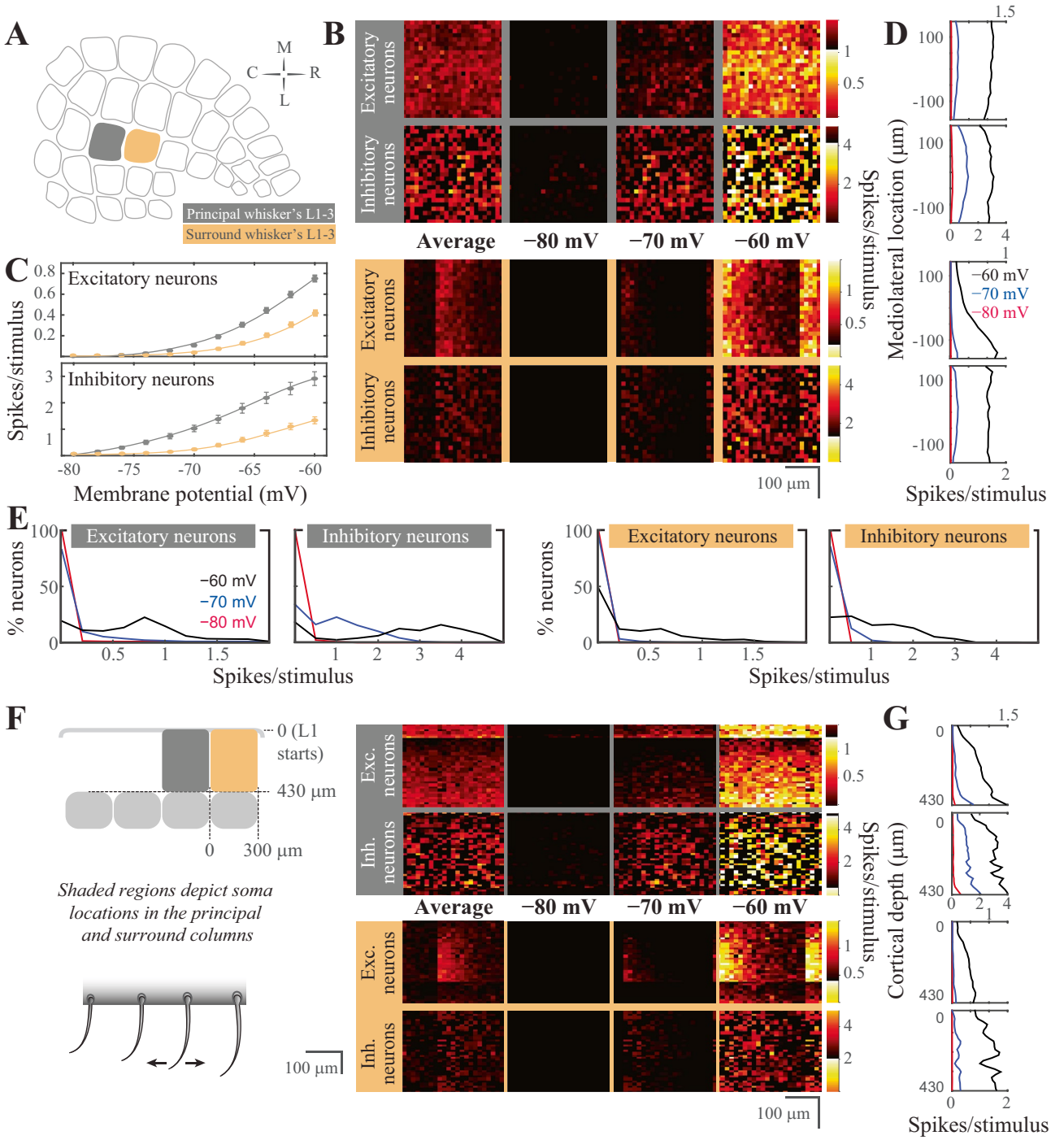

Fig. 5 Stimulus evoked representations in the supragranular layers of the barrel cortical network in silico. (**A**) Schematic representation of the spatial orientation of the simulated network in the tangential plane. The principal cortical column is the D2 whisker's column. (**B**) Average neuronal response mapped onto rostro-caudal (RC) and medio-lateral (ML) planes, across resting membrane states (pixel size 15×15 µm in cortical tissue). The figurines on the grey shaded background display the response in the principal whisker's cortical column; yellow background shows the activity in the first order surrounding supragranular layers. (**C**) Average firing rate of excitatory (top) and inhibitory neurons (bottom) in the network as a function of the resting membrane potential before stimulus onset in the principal (top) and surround (bottom) whisker's cortical network. (**D**) Average firing rate in the ML axis across the membrane states (i.e. each column in B was summed, then rotated 90 degrees). (**E**) Distribution of the spiking response per stimulus across neuron classes and membrane states. (**F**) Left: Schematic representation of the coronal orientation of the visualized network. Right: Average neuronal response across the dorsoventral plane in L4 (pixel size 15×15 µm in cortical tissue). (**G**) Average firing rate across cortical depth

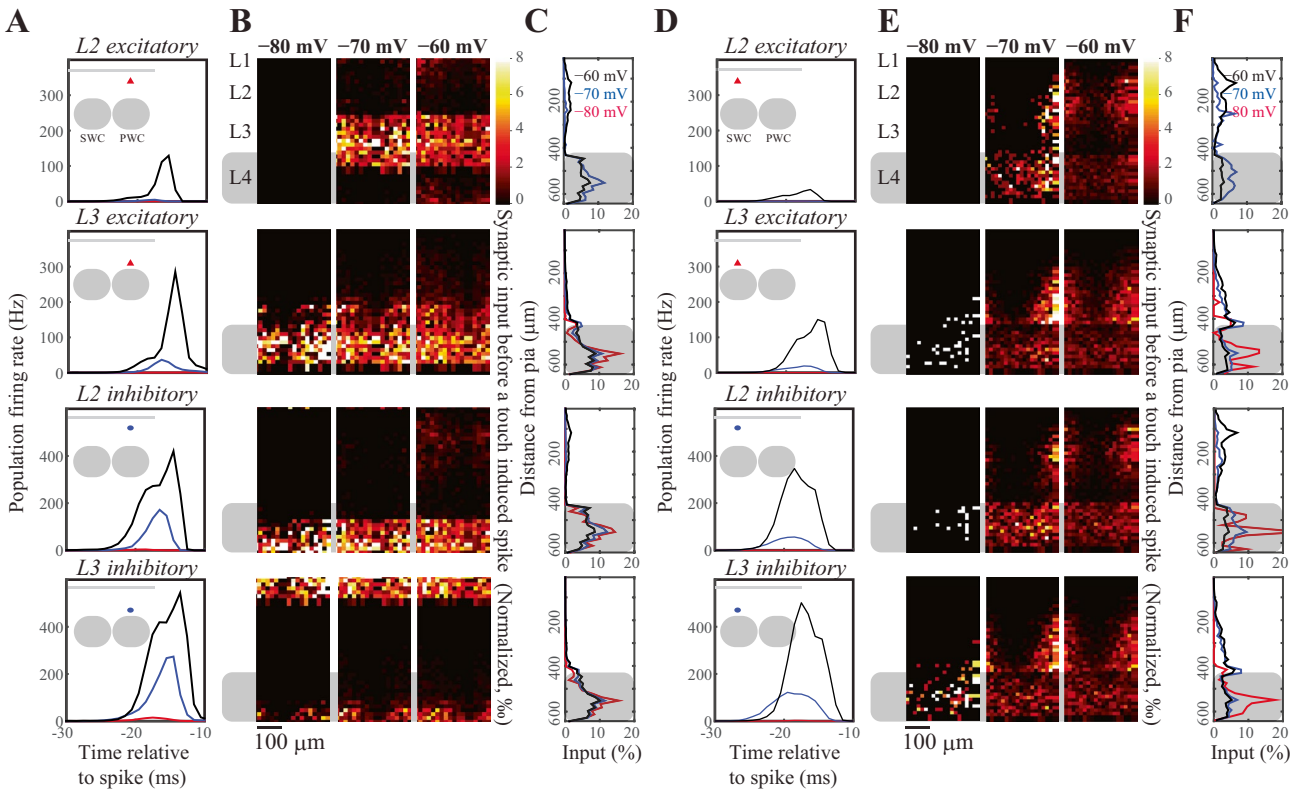

Fig. 6 Visualization of the presynaptic population contributing to a postsynaptic action potential. We spatially mapped the neural activity across the granular and supragranular layers prior to an action potential in a given layer. These postsynaptic spike-triggered maps were averaged across all postsynaptic neurons that fire evoked action potentials during the simulations. (**A**) Population activity that drives L2 excitatory (first row), inhibitory (second row), L3 excitatory (third row) and L3 inhibitory (last row) neurons to spike in response to thalamic input. The first spike fired by aforementioned L2 or L3 neurons was used as the trigger to calculate the spike-triggered input map. Insert: schematic representation of the location of different cell populations in the barrel column. (**B**) Spike triggered spatial averaging (rows as in A); columns denote network activity observed across different resting membrane potentials. (**C**) Average (over time, trials and neurons) depth distribution of excitatory inputs to drive a spike (rows as in A). (**D**-**F**) Same as A-C, but using surround whisker stimulation (SWC) instead of principal whisker stimulation (PWC). The pixels in the spike-triggered maps are normalized as follows: the intensity I (a.u.) for each pixel j is calculated: $I_j = \int_{t_{start\ simulation}}^{t_{postsynaptic\ spike}} \sum_{all\ presynaptic\ neurons\ i\ in pixel\ j} \rho_i(t)dt$, where $\rho_i(t)$ is the spike train of presynaptic neuron i (so each spike adds 1 to the sum). Next, this is averaged over all postsynaptic neurons and all pixels to get to the ratio r of pixel j: $r_j = (\langle I_j / \sum_{all\ pixels\ n} I_n \rangle_{all\ postsynaptic\ neurons}$.

changes in neural representations of touch in silico. Figure 7 shows the implementation of the model on a 3-column model of the barrel cortex, layers 2–4 (Fig. 7A). Each column receives its major synaptic input from its own respective whisker in the form of thalamic representations of whisker touch (see above), with the exception that the center column lacks a principal whisker, mimicking the whisker deprivation condition (Fig. 7B).

Employing empirically observed pairwise STDP rules in synapses at the feed-forward projections originating from L4 (Fig. 7C; bottom) and the intracolumnar projections of L2/3 (Fig. 7C; top) resulted in a reorganization of touch representation already within 100 trials, in agreement with the experimental observations in barrel cortical slices (Allen et al., 2003; Celikel et al., 2004). The model correctly predicted all the known pathways that are modified upon whisker deprivation including the potentiation in the spared whiskers' L4-L2/3 projections (Clem et al., 2008), slow depression in the deprived cortical column's L4-L2/3 projections (Bender et al., 2006) and plasticity of the oblique projections from L4 onto the neighboring L2/3 (Hardingham et al., 2011). The model further predicted a number of circuit changes, including the bidirectional changes across the cross-columnar projections between the spared and deprived columns, which could potentially explain the topographic map reorganization by receptive field plasticity.

Network Representation of Touch in Vivo

As a final test of our in silico cortical column, we let it respond to an in vivo-like stimulation (Fig. 8)*:* as input to the network, we used recorded whisker angle (black) and curvature (red) from a freely whisking rat in a pole

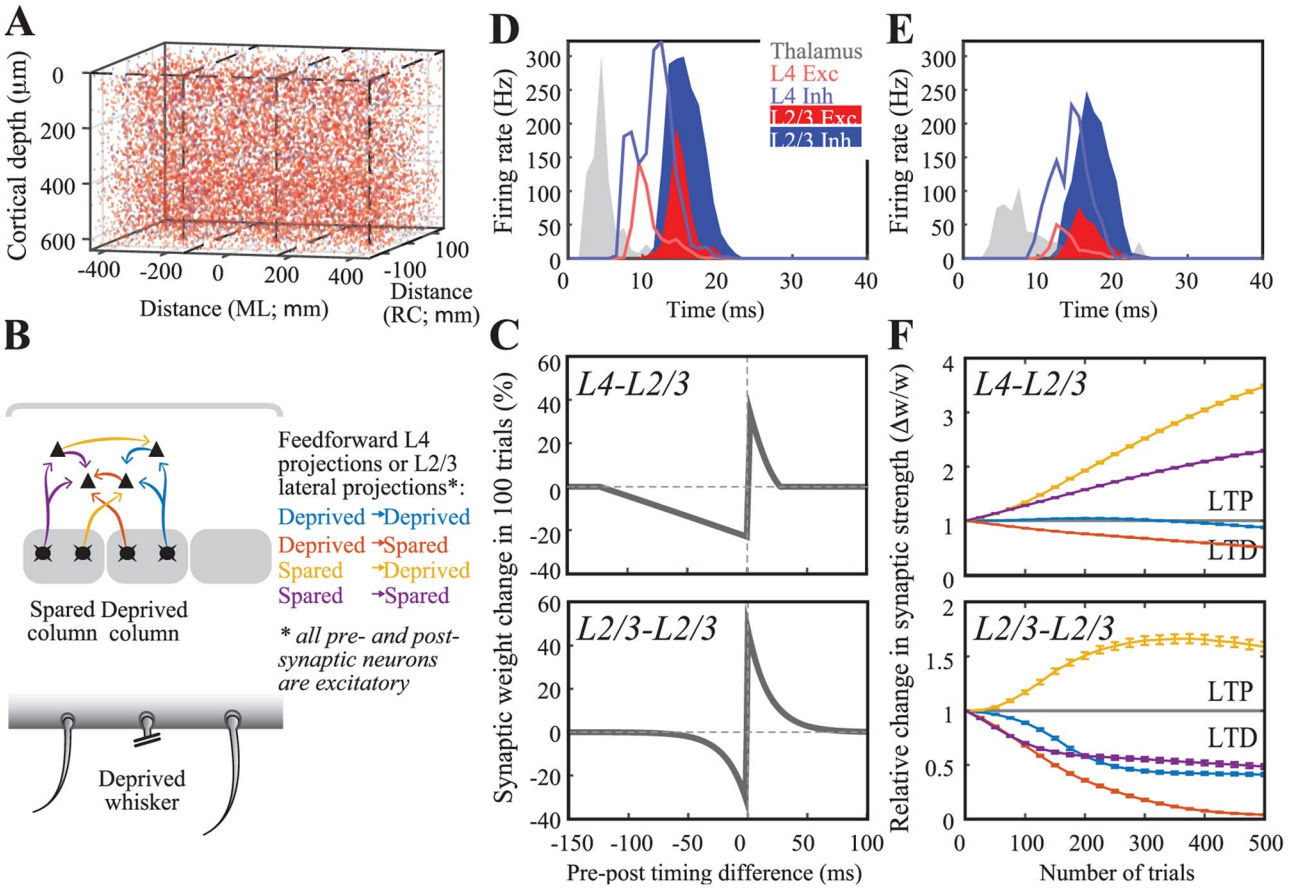

Fig. 7 Spike-timing dependent map plasticity in silico. (**A**) A network model with 3 barrels. Cells in each column are randomly generated using distributions quantified in Fig. 1. (**B**) Schematic representation of the feed-forward and intracolumnar networks in the upper layers of the somatosensory cortex. (**C**) Experimentally observed STDP learning rule in L4-L2/3 projections (top; Celikel et al., 2004; see Materials and Methods) and for L2/3-L2/3 connections (bottom; Banerjee et al., 2014). (**D**) Population PSTH for the spared columns, i.e. most medial and most lateral columns in A1. (**E**) Population PSTH for the deprived, i.e. center, column. (**F**) Change in synaptic efficacy as a function of whisker deprivation in the simulated network. Color codes denote the whisker deprivation status of pre- and postsynaptic neurons' location. Note that presynaptic neurons are always located in L4

localization task (data from (Peron et al., 2015)) made available as 'ssc-2' on CRCNS.org). We modeled thalamus as a network of 3 barreloids, each containing 200 'filter-and-fire' neurons that respond to whisker angle, curvature, or a combination of both. The center barreloid was considered to be the principal barreloid for the spared whisker, whereas the other two were considered surround barreloids, with reduced probability (30% of original amplitude) and delayed (2.5 ms) response latency (Brecht & Sakmann, 2002; Brecht et al., 2003). The response of the network is tightly localized, both in time and place (Fig. 8C, D). The network response is also quite sparse (Fig. 8B, E), with each neuron firing at most a few spikes per trial. This response is a bit more sparse than typically observed (Peron et al., 2015), probably due to the lack of motor and top-down input in this model.

We compare the activity of a single barrel with evoked responses visualized using 2-photon imaging of calcium dynamics (Vogelstein et al., 2009). Although making a neuron-by-neuron comparison between networks is impossible, we can compare the overall activity of the networks. In both the recorded and the simulated networks, the activity is extremely sparse. The simulated network appears to have a few more neurons with a high firing frequency (Fig. 9G), however, these do not adapt their firing frequency upon touch (Fig. 9H), so they probably do not represent touch information (Peron et al., 2020). Otherwise, both networks show a comparable overall activity pattern.

Discussion

Understanding the circuit mechanisms of touch will require studying the somatosensory cortex as a dynamical complex system. Given that the majority of research in the barrel system has thus far focused on the identification

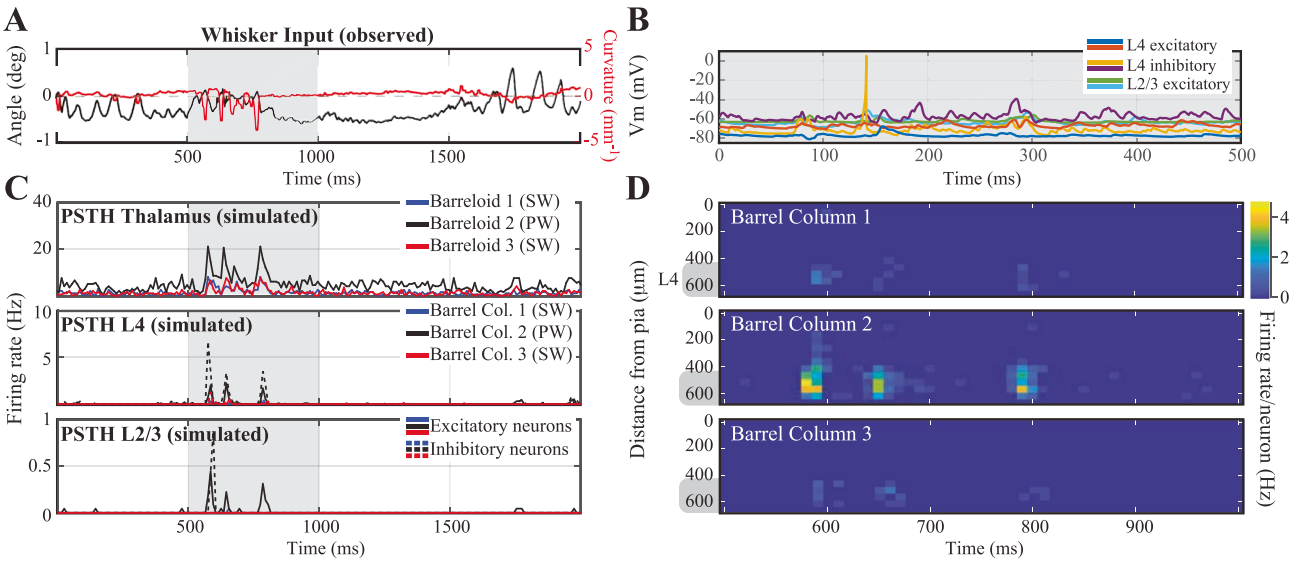

Fig. 8 Network response to in vivo-like stimulation. (**A**) Input to the network: whisker angle (black) and curvature (red) from a freely whisking rat in a pole localization task (data from (Peron et al., 2015), made available as 'ssc-2' on CRCNS.org). (**B**) Example voltage trace responses of 6 randomly chosen model neurons. (**C**) Peri-Stimulus Time Histograms (PSTHs) of the model-thalamus (top), L4 (middle) and L2/3 (bottom). The thalamus consists of 3 barreloids, each containing 200 'filter-and-fire' neurons that respond to whisker angle, curvature or a combination of both. The central barreloid (black, 2) receives a stronger input, as this is the 'stimulated' barrel for the only spared whisker. Spike trains of the thalamus are sent to the cortical network model of L4 (middle), which sends its spike trains to L2/3 (bottom). These similarly consist of 3 barrels, of which the central (black, 2) barrel belongs to the spared whisker. (**D**) Average membrane potential of the excitatory (left) and inhibitory (right) model neurons as a function of cortical depth. L4 (barrel cortex) is denoted with a grey shaded shape. (**E**) Average firing rates of the model neurons as a function of cortical depth

of circuit components the development of a computational model of the barrel cortex is not only necessary but also feasible. Accordingly, we here employed a three-tiered approach to (1) reconstruct the barrel cortex in soma resolution, (2) implement a model neuron whose spiking is a function of the network activity impinging onto postsynaptic neurons, and (3) axo-dendritically connect neurons in the column based on Peter's rule and experimentally observed pairwise network connectivity (see Materials and Methods). We finally performed simulations in this network to compare neural representations of touch in silico to experimental observations from biological networks in vivo. As extensively discussed in the Results section, the simulations faithfully replicate experimental observations in vivo with high accuracy including, but not limited to, emergence of whisker representations, experience-dependent changes in synaptic strength and circuit representation of touch from behavioral data, using information from whisker displacement during tactile exploration. Thus, here we will focus on the methodological limitations and technical constraints of the network modeling as performed herein.

Technical Considerations for Anatomical Reconstruction of a Stereotypical Barrel Column

One of the essential steps towards building a biologically plausible *silico* model of the mouse barrel cortex is to obtain the distribution patterns of different neuron types throughout the barrel cortex. In the current study, we directly visualized these distributions by labeling different types of neurons using cell-type specific markers and digitized the data using confocal scanning microscopy to ultimately reconstruct the cortex in soma resolution upon automated counting of all neurons, independent from whether the markers are nuclear or cytoplasmic. The identities of individual barrels in L4 can be reliably recognized based on GAD67 immunostaining (Supplemental Fig. 3). However, due to difficulties in aligning images across consecutive sections, we could not consistently follow every barrel column across the entire cortical depth. Thus, in the current study, we only report average cell densities across a canonical barrel cortex rather than reconstructing the barrel cortex while preserving the columnar identity. Similarly, the in silico model places neurons and synapses stochastically

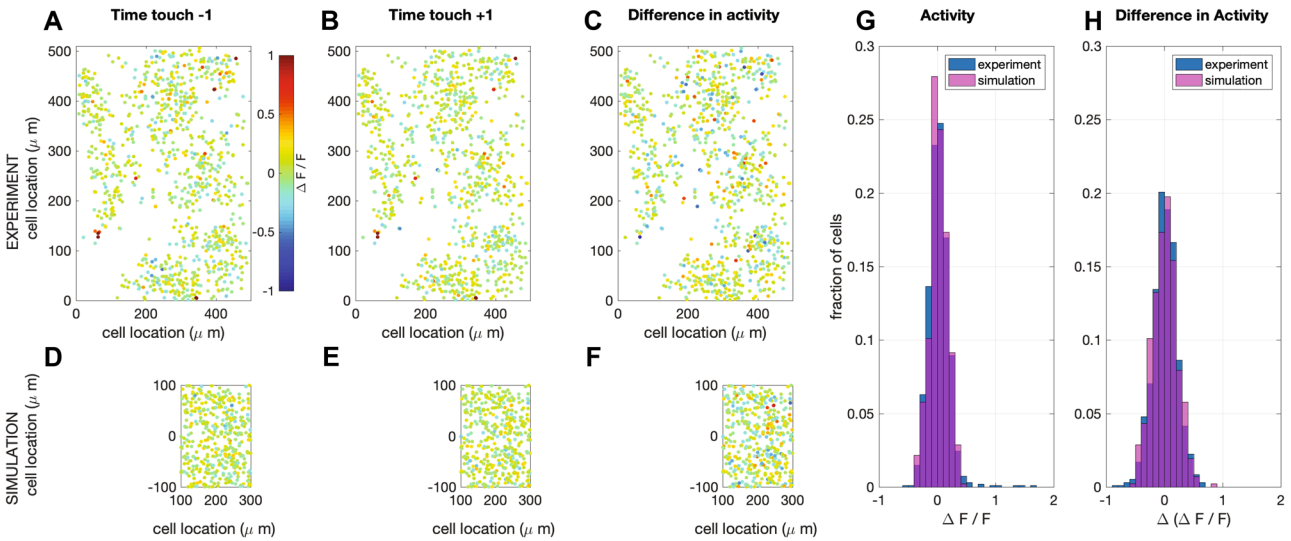

Fig. 9 Simulation of calcium imaging experiment in L2/3. (**A**) Recorded (Peron et al., 2015) network response one (time) frame before touch (sampling frequency: 7 Hz; recorded volume: 6). (**B**) Recorded network response one frame after touch **(C)** Difference in network response between before and after touch. (**D**-**F**) Same as in A-C, but now for simulations (full simulation: single barrel including L23 (shown here) and L4 (see supplemental Fig. 4). The fluorescence signal was calculated from network response following the method in (Vogelstein et al., 2009) (see Materials and Methods). Note that a recorded volume is larger than a single barrel. The frames are scaled accordingly. (**G**) Comparison of the distribution of activity of one frame after touch between the recorded and the simulated network. (**H**) Comparison of the distribution of the difference in activity between one frame before and after touch between the recorded and the simulated network

every time a network is reconstructed, reflecting this inherent uncertainty. The advantage of this is, that simulations can be repeated over different realizations of networks with a similar structure, and this way it can be tested whether results are a general property of such networks or just a coincidental result of a particular realization of the network. It should be noted that, in the rat barrel cortex, the cell density across different barrel columns has been shown to be relatively constant (Meyer et al., 2013), making our density estimation likely to be accurate, as we employed a normalized volume for the entire column. Obviously, however, the absolute cell number in one barrel column could vary depending on the exact location of the barrel within the barrel cortex (Meyer et al., 2013).

Our automatic cell counting algorithm for nuclear cell counts is functionally similar to that employed in (Oberlaender et al., 2009). Compared to their method, we used lower threshold values to separate foreground objects from their background in order to capture weakly stained cells. This comes at the expense of an increased number of connected clusters. We thus employed more sophisticated methods to separate clusters of connected cells, based on both intensity and shape information, rather than simply assuming that there exists a single dominant cell population based on volume, which could lead to bias when the assumption is not met (Oberlaender et al., 2009). Our method does not require manual correction, and the counting results are comparable with manual counts (Supplemental Table 5). Furthermore, we also developed algorithms to enable source localization for the cytoplasmic signals, which allowed us to quantify cellular classes, like somatostatin neurons, that are characterized by non-nuclear markers. Together these approaches have resulted in the most detailed quantification of the network, going beyond the two-neuron group (i.e. excitatory vs inhibitory) clustering available in the literature.

Tissue shrinkage could affect cell density estimates. Although we project cell densities onto a normalized volumetric column, and although we have quantified the shrinkage of the sections, the cell density estimates might somewhat differ using alternative reconstruction methods. Another potential error could be introduced by cutting cells located at slice borders – these cells will appear in both slices, resulting in an overestimation of the cell count. We corrected for this overestimation by including only those cells within a given radius along the z-direction (which is orthogonal to the cutting plane) and no smaller than half of the average radius along x- and y-direction. This ensured that the overwhelming majority of the cells were not counted twice, as confirmed by the human observer quantifications.

Comparison with Past Cell Counts

In our data, the average neuronal density, as identified by NeuN staining, across all layers of the mouse barrel cortex is 1.66×10^5 per mm^3, before correcting for tissue shrinkage. Assuming that each slice in our sample was cut precisely as a 50 µm section, after immunostaining the average optical thickness of slices was reduced to 32.5 µm, indicating a 34.8% shrinkage in z-direction. The shrinkage along x–y plane was generally much smaller in our protocol: imaged cells with a voxel size of 0.73-by-0.73-by-0.45 or 1.46-by-1.46-by-0.9 µm showed similar pixel radius along x-, y- and z- axes (data not shown). If we assume that the real neurons have a similar radius along the 3 axes, the data suggests a shrinkage factor of ~ 2.3% along x- and y- axes. After correcting for the estimated average shrinkage factors, the average neuronal density became 1.03×10^5 per mm^3, in agreement with the previous observations made in the C57B6 mouse (i.e. 0.6×10^5–1.6×10^5 per mm^3, (Hodge et al., 2005; Irintchev et al., 2005; Lyck et al., 2007; Ma et al., 1999; Tsai et al., 2009)).

Comparison with Other Simulated Networks

Network models help explain network dynamics and information processing on many levels. Therefore, they exist at many different scales of complexity. On one extreme, simplified network models investigate how a single or a few aspects of the network (connectivity) properties affect network behavior. For instance, randomly connected balanced networks use integrate-and-fire neuron models (Brunel, 2000), binary neuron models (van Vreeswijk & Sompolinsky, 1996, 1998), or rate neuron models (Sompolinsky et al., 1988) to investigate the effects of synaptic sparseness, connectivity strength and the balance between excitation and inhibition on network dynamics. Similarly, like discussed in the introduction, feed-forward networks like the perceptron (Rosenblatt, 1958) can explain the increasing abstraction of receptive fields in sensory perception using similar simplified neuron models (Seung & Yuste, 2012) and randomly connected symmetric networks (Hopfield, 1982) can explain associative memory. Finally, the dynamics of small-world networks (Watts & Strogatz, 1998) have several special properties such as rapid (near-critical) synchronization, low wiring costs and a balance between locally specialized and large-scale distributed information processing (Bassett & Bullmore, 2006; Stam & Reijneveld, 2007).

Although simplified networks are often very powerful in providing (analytical) explanations about the influence of connectivity on network behavior, they are biologically not very realistic. A middle ground can be found in biologically-inspired networks that use the intrinsic connectivity schemes found in the brain. These model networks often make specific predictions about the effects of network properties on dynamics, although analytical solutions are mostly not feasible (see for instance Rubin & Terman, 2004; Tort et al., 2007; Wendling et al., 2002)).

Another intermediate level of network modeling involves fitting functional models to whole-network recordings (e.g. Generalized Linear Models (GLMs) (Paninski, 2004; Pillow et al., 2008; Truccolo et al., 2005), Generalized Integrate-and-Fire models (GIF models) (Gerstner & Kistler, 2002; Jolivet et al., 2004)). With these types of models, the spiking behavior and functional connectivity of entire networks can be fitted to network recordings. The results from such an analysis can be difficult to link to biophysical properties of the neurons and networks, but it is a very successful method for describing the functional connectivity of for instance the macaque, salamander, cat and rabbit retina (Denk & Detwiler, 1999; Doi et al., 2012; Keat et al., 2001; Li et al., 2015; Marre et al., 2012; Pillow et al., 2008; Reich et al., 1998) (for a review see (Field & Chichilnisky, 2007)) and C. elegans (Kato et al., 2015).

Finally, on the other extreme, are biologically reconstructed networks, like the one we present here. For some systems, complete or partial wiring diagrams have been published (C. elegans (Varshney & Chen, 2011), mouse retina (Helmstaedter et al., 2013)), that can be used to construct such models. A notable example is the crustacean stomatogastric ganglion system, that has been extensively studied and simulated, leading to variable invaluable insights into neural network functioning in general (Marder & Goaillard, 2006; Prinz et al., 2004). These networks are biologically realistic, but because of their complexity, it is more difficult to analyze the influence of specific network properties on network dynamics and function. Moreover, one concern is that with the current methods, it is still impossible to measure all relevant parameters (molecular cell-type, electrophysiological cell-type, cell location, structural connectivity, functional connectivity) in a single sample. Therefore, every biologically reconstructed network so far is a combination of properties from different individuals and even animals. Whether such a synthesized model is a good approximation of the actual functional neural network remains to be seen (Edelman & Gally, 2001; Marder & Taylor, 2011). Moreover, all current reconstructed networks are limited in their scope: right now it is not feasible to reconstruct and model the whole brain. For the barrel cortex presented here, that means that amongst others motor and top-down input are missing, which results in a reduced neural activity in silico compared to observed experimentally (compare Figs. 8 and 9 to (Peron et al., 2015)) especially during hyperpolarized membrane potentials. Moreover, on-going activity in these areas is a major source of response variability in vivo. Other mechanisms that we decided not include are the history dependence of synaptic failures (Beierlein et al., 2003), the shape

(steepness of the upstroke) of the action potentials (Badel et al., 2008; Gutkin & Ermentrout, 2006; Harrison et al., 2015) and gap junctions (Beierlein et al., 2003; Gibson et al., 1999; Tamás et al., 2000). Despite these limitations, biologically reconstructed network models are very important as a testing ground for hypotheses based on more simplified networks, or to assess biological parameters that are difficult or impossible to measure experimentally, such as the effects of threshold adaptation (Huang et al., 2016; Zeldenrust et al., 2020) or the effects of different coding schemes (Huang et al., 2020). In Supplemental Table 1, we have summarized the properties of several biologically reconstructed networks that have been published. Note that until now, many of these reconstructed networks have to be run on a cluster of computers or on a supercomputer, because a simple desktop computer simply lacked the computational power to run a biologically reconstructed network and/or did not make the code available (Tomsett et al., 2015) being an exception). We used simplified neuron models instead of reconstructed multi-compartmental models, increasing the computational efficiency,[1] but possibly missing effects due to the morphology, such as certain forms of bursting (Zeldenrust et al., 2018), dendritic computation (Chu et al., 2020) or axon-initial segment effects (Kole & Brette, 2018). The NetPyNE implementation of the model presented here allows for easy replacement of the neuron models, allowing for a further exploration of the influence of a diversity of neural properties on the network activity. Finally, like the recent model by Markram et al. (Markram et al., 2015), we used no parameter tuning to construct this model, other than making the different cell-types of the Izhikevich-model and controlling the cell-type specific connection probabilities. All this makes the model very accessible for quickly testing fundamental hypotheses systematically (Huang et al., 2016, 2020).

Materials and Methods

Experimental Procedures

Tissue Preparation and Immunochemistry

The slices from the barrel cortex were described before (Kole et al., 2020; Kole & Celikel, 2019) with minor modifications. In short, juvenile mice from either sex were perfused using 4% paraformaldehyde before tangential sections were prepared. To ensure that cortical layers were orthogonal to the slicing plane the cortex was removed from the subcortical areas and medio-lateral and rostro-caudal borders trimmed. The remaining neocortex included the entire barrel cortex and was immobilized between two glass slides using four 1.2 mm metal spacers. The rest of the histological process, including post-fixation and sucrose treatment, was performed while the neocortex was flattened. All care was given to ensure that the tissue is as flat as possible at the time of placement onto the sliding horizontal microtome. 50-micron sections were cut and processed using standard immunohistochemical protocols. The following antibodies were used: anti-NeuN (Millipore, Chicken), anti-GAD67 (Boehringer Mannheim, Mouse), anti-GABA (Sigma, Rabbit), anti-Parvalbumin (PV, Swant Antibodies, Goat), anti-Somatostatin (SST, Millipore, Rat), anti-Calretinin (CR, Swant Antibodies, Goat), anti- vasointestinal peptide (VIP, Millipore, Rabbit) at concentrations suggested by the provider.

The imaging was performed using a Leica Confocal microscope (LCS SP2) with a 20X objective (NA 0.8). Each section sequentially cutting across layers was individually scanned with 512×512 pixel resolution; the signal in each pixel was average after 4 scans and before it was stored. The alignment of each section was performed automatically using a fast Fourier transform based image registration method (Guizar-Sicairos et al., 2008).

Automated cell counting

All image analysis was done using a custom-written running toolbox in Matlab 2012b with an Image Processing Toolbox add-on (Mathworks).

Nucleus-Staining Channels (NeuN, Parvalbumin and Calretinin)

Most fluorescence imaging methods, including confocal microscopy, have several shortcomings that make the automated cell identification a challenging task: First, the background intensity of images is often uneven due to light scattering and tissue auto-fluorescence. Shading and bleaching of fluorophores further add to this problem when acquiring multiple confocal images at the same location. Second, intensity variation within a single cell might cause over-segmentation of the cell. Third, the intensity of different neuron populations turn out to be very different because they absorb fluorescent dye unevenly. Specifically, GAD67 + and SST + neurons usually have a weakly stained nucleus as visualized by anti-NeuN antibody, making non-linear gain modulation necessary in a cell-type specific manner. To overcome these problems and maximize the hit and correct rejection rate over miss and false positives (i.e. (H + CR)/(M + FP)), we have developed the following pipeline:

[1] For example, the Matlab model, ran on a MacBook Pro laptop with a 2.4 GHz 8 core processor and 32 Gb RAM took about 1 h to create a 1-barrel model, and then about a minute to run a 6 s simulation; it took about 6.5 h to create a 3-barrel model and then 6 min to run a 6 s simulation.

Pre-processing: The goal of pre-processing is to obtain relatively consistent images from original fluorescent images with varying quality to pass to the cell count algorithm, so the same algorithm can process a large variety of images and still get consistent results. Depending on the nature of the individual channel, i.e. which antibody was used, different pre-processing steps were employed.

Median filtering: A median filter with $3 \times 3 \times 3$ pixel neighborhood is applied to fluorescent image stacks to smooth intensity distribution within each image stack in 3D. This operation removes local high-frequency intensity variations (Supplemental Fig. 1b).

Vignetting correction: Vignetting is the phenomenon of intensity attenuation away from the image center. We use a single-image based vignetting correction method (Zheng et al., 2009) to correct for the intensity attenuation (Supplemental Fig. 1c). The algorithm extracts vignetting information using segmentation techniques, which separate the vignetting effect from other sources of intensity variations such as texture. The resulting image is the foreground, i.e. the cellular processes, on a homogenous background.

Background subtraction: Background can result from non-specific binding of antibodies or auto-fluorescence of the tissue. To reduce the background noise, local minima in each original grayscale image are filled by morphological filling, and background is estimated by morphological opening with 15 pixel radius disk-shaped structuring element. The radius value is chosen to be comparable to the largest object size so the potential object pixels are not affected. The estimated background is then subtracted from the original image to enhance signal-to-noise ratio, SNR (Supplemental Fig. 1d).

Contrast-limited adaptive histogram equalization (CLAHE): CLAHE (Heckbert, 1994) enhances local contrast within individual images by remapping intensity value of each pixel using a transformation function derived from its neighbourhood. While increasing local contrast and amplifying weakly stained cells, it also reduces global intensity difference, which partially corrects for the uneven illumination that individual fluorescent images often suffer from (Supplemental Fig. 1e). CLAHE is applied as an 8×8 tiles division for each image. Images from channels with very low number of positive staining with high SNR (e.g. Calretinin staining channel) are not processed with CLAHE.

Image Segmentation to Identify Cell Nucleus

Black-and-white image transform is applied to grayscale images to separate foreground, i.e. regions presumably contain nuclei, from background. In the ideal conditions, if all the objects were stained evenly during immunochemistry, the image pixels' intensity value will be distributed as two well-separated Gaussian distributions. However, objects are usually not evenly stained; specifically, GAD67 + and SST + neurons usually have weak NeuN staining. As a result, the intensity distribution for object pixels is very broad and cannot be described by a single Gaussian distribution. To reliably identify foreground pixels we calculated threshold values using 2-level Otsu's method (Otsu, 1979), which separates the pixels into 3 groups. The group with the lowest intensity reliably captures the background pixels, and the other 2 groups are set to the foreground. This transformation is directly applied to 3D image stack to obtain 3D foreground (Supplemental Fig. 1f).

Marker-based watershed segmentation: B&W transform identified regions contains cell nucleus, albeit non-specifically, and it does not identify the location and shape of each individual nucleus stained, thus image segmentation is needed to identify individual nuclei. Watershed method (Meyer, 1994) is an efficient way of segmenting grayscale images, i.e. foreground part of image obtained by B&W transformation based on gradient, and has the advantage of operating on local image gradient instead of global gradient. However, direct application of watershed methods usually results in over-segmentation of nuclei due to local intensity variation within individual nuclei. To overcome this problem, marker-based watershed algorithm is employed, in which markers serving as starting 'basin' for each object are first placed on an image to be segmented, and watershed algorithm is then applied to produce one segment (or object) on each marker.

We computed the markers by applying regional maxima transform on foreground grey-scale images. To ensure at most one marker is placed in each nucleus, first the grey-scale image need to be smoothed to eliminate local intensity variation. This is realized by applying morphological opening-by-reconstruction operation (Vincent, 1993) with 5 pixels radius on foreground grayscale image, which removes small blemishes in each individual nucleus and ensures regional maxima transform can find foreground markers accurately.

After identifying markers watershed algorithm is applied (Supplemental Fig. 1g). To ensure accurate detection of cell boundaries, the B&W foreground needs to enclose the entire cell object. This image dilation is applied to the B&W foreground to enlarge it by 1 pixel in radius before application of watershed segmentation algorithm. Finally, objects with size smaller than 400 pixels in total are removed by morphological opening.

Corrections for clusters of connected neurons: Clusters of closely located neurons are not always successfully separated without further image processing; especially when closely located neurons all have similar intensity distribution. In such cases application of intensity-based watershed algorithms result in identification of one object instead of many

real neurons (Supplemental Fig. 1b). Furthermore, our strategy for watershed segmentation to augment regional intensity similarity to make sure that nuclei are over-segmented actually increases the chance of under-segmentation during clustering. To correct for this under-segmentation we employed a five-step approach:

a. The volume (total number of pixels) of all identified objects is calculated, and objects with a volume larger than mean + std of the population are labeled as "potential clusters".
b. For each object in the potential cluster list, the original grayscale image is retrieved. Then, from all the pixels contained in the object, 50% pixels with lower intensity values are removed, generating a new B&W object with a smaller size. Because usually, those low-intensity pixels are from the periphery region of each individual neuron, the new B&W object has better separation between different neurons.
c. Euclidean distance-based 3-D regional maximum transform is then applied to the new, smaller B&W 3-D candidate object, in which the distance from each pixel belongs to the object to the border of the object, is calculated. Assuming neurons have Ellipsoid-like shape, the peak (largest distance from borders) of this transform will likely be the center of neurons, even if they are connected. The regional maximum transform is then applied to locate those peaks in the Euclidean distance space. Before the regional maximum transform is applied, the target image is smoothed by morphological opening-by-reconstruction operation with 1-pixel radius to remove small local variations.
d. If more than one center is found (in c) watershed method is applied to the distance transform of the original B&W object, using the identified centers as markers. If only one center is found then the cluster is judged as a single neuron and removed from the list. Again, the distance metric is smoothed by a morphological opening-by-reconstruction operation before the watershed algorithm is applied.
e. Steps a-d is repeated until the "potential cluster list" is empty (Supplemental Fig. 1h).

Morphological filtering: Neurons have a certain shape and volume. Based on this statistical information clustered objects can be filtered to remove small artifacts. This is necessary because of the low threshold value used for the foreground generation. To remove the artifacts from neurons we first performed a morphological opening with a structure whose size is 1/3 of the size of each object's bounding box. The bounding box is calculated in 3-D hence it is the smallest cube that contains the object. This operation breaks down irregular shapes but keeps relatively regular shapes (sphere, ellipsoid, cuboid) intact. Then, both pixel size (volume) and mean intensity of the objects are fitted with a Gaussian mixture model, and the group with the smallest pixel size and lowest mean intensity is judged as an artifact and is removed. (Supplemental Fig. 1f).

Combining information from different soma-staining channels: Cells identified from each channel are added together to give cumulative soma counts across all antibody channels. Overlapped objects are judged to be different cells if:

a. Overlapping is smaller than 30% of any object volume constituting the cluster
b. after subtraction the new object preserves the ellipsoid shape

Cytosol-Staining Channels (GAD67 and Somatostatin)

Identification of the cells in cytosol-staining channels utilizes reference information gathered from the soma-staining channels, hence segmentation of cytosolic signals requires at least one nuclear channel staining.

Early stages of the image processing for the cytosolic signal localization was identical to that of soma-staining channels except CLAHE step. Subsequently, cell objects were imported from combined soma-staining channels information (Supplemental Fig. 2c).

For each cell object, two additional pixels were added to the diameter of the object (Supplemental Fig. 2d). This enlarged cell object is used as a mask to detect positive staining in the cytosol-staining channel (Supplemental Fig. 2f). Positive staining was defined as connected pixels with a volume at least 10% of the object and that they have significantly higher intensity compared to the pixels within 2.5 times of the associated cell (Supplemental Fig. 2g). Finally, the percentage of positive staining was obtained and used to identify GAD67 or Somatostatin positive cells.

Performance comparison between computer and the human observer.

Three human observers independently counted a number of 3-D images stacks from different antibody staining, using Vaa3D software (Peng et al., 2010). Three identical copies of each image stack were placed in the manual counting dataset in random order; the human observers subsequently confirmed that they did not notice the duplicates in the data set they had analyzed. The automated counting result was compared with the average human counting result, and the summary of the difference is shown in Supplemental Table 5.

Generating an Average Barrel Column

After performing automatic cell counting on individual slices across different cortical depths, we calculated average cell density for different types of cells identified by distinct antibody channels at a given cortical depth as indicated by slice number. Tissue shrinkage was not corrected but the average column size was empirically determined. To account for the differences in cortical thickness across different animals, we then binned the density data from each individual animal into 20 bins, which were subsequently averaged to obtain the average cell density distribution across cortical depth. The layer borders z_{lim} between different cortical layers (L1-L2/3, L2/3-L4, L4-L5, L5-L6) were determined as described previously (Meyer et al., 2010), by first fitting a Gaussian function

$$g(z) = c_1 + c_2 e^{-(z-z_0)^2/2\sigma^2}$$

to the NeuN + cell density profile along with cortical depth with manually set c_1, c_2 and z_0, and then the respective z_{lim} was calculated as

$$z_{lim} = z_0 \pm \sigma\sqrt{2\ln 2}$$

L5A-L5B border was determined by manual inspection on NeuN + cell density. We then calculated the size of an average barrel in C-E rows, 1–3 columns by manually labeling corresponding barrels in anti-GAD67 staining (Supplemental Fig. 3). The number of different types of cells in an average barrel from C-E rows, 1–3 columns was then calculated by the size as well as the corresponding cell density.

Network Setup

Neuronal Model

We used the Izhikevich quadratic model neuron (Izhikevich, 2003, 2004) in this study:

$$\frac{dv}{dt} = 0.04\left(v - v_r\right)\left(v - v_t\right) - u + I$$

where v, v_r, and v_t are the membrane potential, resting membrane potential without stimulus, and the spike threshold of the neuron, respectively and I is the synaptic current the neuron received (see below). The dynamics of the recovery variable u are determined by:

$$\frac{du}{dt} = a(b\left(v - v_r\right) - u)$$

Parameters a, b, c, d together determine the firing pattern of the model neuron (see Supplemental Table 4). The model has the following reset condition:

$$\text{if } v \le 30 \begin{cases} v \leftarrow c \\ u \leftarrow u + d \end{cases}$$

Parameters a, b and c were taken from (Izhikevich, 2003); parameter d was adapted to match firing rates observed in the literature. Heterogeneity was included by drawing the parameter values from random distributions around these values (see Supplemental Table 4 for the parameter values, Supplemental Table 3 for the relevant literature). For the simulations in Matlab, a first-order Euler method with a step size of 0.1 ms was used. For NetPyNE, the built-in solver was used.

The Izhikevich neuron model is one of many 2D spiking neuron models, i.e. point neuron models with an membrane potential variable and a slow adaptation variable, a group of models that includes the AdEx model (Brette & Gerstner, 2005), the Morris-Lecar model (Morris & Lecar, 1981) and more. All these models are shown to have a high accuracy in reproducing cortical spike trains, as long as the slow adaptation parameter is included (Botella-Soler et al., 2018; Brette & Gerstner, 2005; Fontaine et al., 2014; Gerstner & Naud, 2009; Jolivet et al., 2004; Jones et al., 2015; Kobayashi et al., 2009; Naud & Gerstner, 2013; Rauch et al., 2003; Rossant et al., 2010, 2011; Woo et al., 2021). In the NetPyNE implementation of this model, the Izhikevich models can easily be exchanged for other point or more extended models.

The threshold θ adaptation was implemented in a simple direct way in Figs. 2–7:

$$\theta(t) = -0.99s - 40.2,$$

where s is the average slope of EPSP in a 5 ms window. In Figs. 8 and 9 we implemented it with the more advanced method (Fontaine et al., 2014), parameter values for each neuron type are in Supplemental Table 6:

$$\tau_\theta \frac{d\theta}{dt} = \theta_\infty(v) - \theta,$$

$$\theta_\infty(v) = \alpha\left(v - v_i\right) + v_T + k_\alpha \log\left(1 + e^{\frac{v - v_i}{k_i}}\right).$$

Unless mentioned otherwise, simulations were initialized with at membrane potential -70 mV, with a small standard deviation of 1.3 mV.

Neural Network Model

The Matlab code of the model, including an example of how to run these simulations can be found in the following GitHub repository:

https://github.com/DepartmentofNeurophysiology/Cortical-representation-of-touch-in-silico.

It can also be found in the Open Source Brain:

https://www.opensourcebrain.org/projects/l4-and-l2-3-of-rodent-barrel-cortex

Moreover, a NetPyNE implementation (exportable to Brian, NEST, NEURON and other platforms through NeuroML and SONATA) can be found here:

https://github.com/DepartmentofNeurophysiology/Cortical-representation-of-touch-in-silico-NetPyne

Neural Distributions

The mouse barrel cortex L4-L2/3 network is modeled based on the distribution of different classes of neurons in an average barrel reconstructed by immunochemical labeling and confocal microscopy (see above). 13 different types of cortical neurons are included in the model (Markram et al., 2004; Oberlaender et al., 2012; Thomson & Lamy, 2007). In L2/3 there are 9 types of neurons, 2 excitatory: L2 pyramidal neurons and L3 pyramidal neurons (Brecht et al., 2003; Feldmeyer et al., 2006); 7 inhibitory: PV + fast-spiking neurons (Holmgren et al., 2003; Packer & Yuste, 2011), PV + bursting neurons (Blatow et al., 2003), SST + Martinotti neurons (Fino & Yuste, 2011; Kapfer et al., 2007; Wang et al., 2004), Neurogliaform cells (Tamás et al., 2003; Wozny & Williams, 2011), CR + bipolar neurons (Caputi et al., 2009; Xu et al., 2006), CR + /VIP + multipolar neurons (Caputi et al., 2009) and VIP + /CR- neurons (Porter et al., 1998). In L4 there are 4 types of neurons, 2 excitatory: L4 spiny stellate neurons and L4 star pyramidal neurons (Egger et al., 2008; Staiger et al., 2004); 2 inhibitory: PV + fast-spiking neurons and PV-low-threshold spiking neurons (Beierlein et al., 2003; Koelbl et al., 2015; Sun et al., 2006). The distribution of excitatory, PV + , CR + , and SST + neurons are taken from the anatomical reconstructions; for other cell types, we assigned corresponding number of different neurons in each cluster based on the previous studies (Kawaguchi & Kubota, 1997; Uematsu et al., 2008). These neurons were distributed in a 640-by-300-by-300 µm region (L4, 210-by-300-by-300; L2/3, 430-by-300-by-300). Note that we scaled the size of the network to match the average dimension of a rat column (Feldmeyer et al., 2006), due to the fact that most of the axonal and dendritic projection patterns were measured in the rat.

Connectivity

Connectivity is determined using axonal and dendritic projection patterns (Egger et al., 2008; Feldmeyer et al., 2002, 2006; Helmstaedter et al., 2008; Lübke et al., 2003) which are approximated by 3-D Gaussian functions, with the assumption that the probability that two neurons are connected is proportional to the degree of axonal-dendritic overlap between these two neurons (i.e. Peter's rule, (White, 1979)). For each pre-synaptic i and post-synaptic neuron j, we calculate the axonal-dendritic overlapping index $I_{i,j}$, which is the sum of the product of presynaptic axonal distribution and postsynaptic dendritic distribution D_j:

$$I_{i,j} = \int_x \int_y \int_z A_i D_j \, dxdydz \; x, y \in SD_j$$

where SD_j is the 3-D space that contains 99.9% of D_j. We then convert $I_{,ij}$ into connection probability $P_{i,j}$ between neuron i and j, by choosing a constant k for each unique pre- and post-synaptic cell type pair so that the average connection probability within experimentally measured inter-soma distances (usually 100 µm) matches the empirically measured values between these two types of cells (Supplemental Table 3):

$$P_{i,j} = k \cdot I_{i,j}$$

Finally, a binary connectivity matrix was randomly generated using the pairwise connection probabilities $P_{i,j}$, in which connected pairs are labeled as 1. Note that the inter-barrel connections follow the same rules, but their connectivity will be lower as these neurons are further apart.

Synapses

Synaptic currents in this network are modeled by a double-exponential function. Parameters of those functions are adjusted to match experimentally measured PSPs (peak amplitude, rise time, half-width, failure rate, coefficient of variation and pair-pulse ratio) in the barrel cortex in vitro (Supplemental Table 3; see (Thomson & Lamy, 2007) for an extensive review). The onset latency is calculated from the distance between cell pairs; the conduction velocity of the action potential was set to 190 µm/ms (Feldmeyer et al., 2002). The short-term synaptic dynamics (pair-pulse depression/facilitation) is modeled as a scalar multiplier to actual synaptic weight, which follows a single exponential dynamic (Izhikevich & Edelman, 2008):

$$\frac{dx}{dt} = \frac{I - x}{\tau_x}, x \leftarrow px \text{ when presynaptic neuron fires}$$

τ_x was set to 150 ms for excitatory synapses and depression inhibitory synapses ($p < 1$), and 100 ms for facilitating inhibitory synapses ($p > 1$). Differences in the activation state of cortex are included in the model by setting the common initial voltage and the equilibrium potential v_r of all cells, thus accounting for potential up-and down-states as well as an intermediate state. The synaptic failures were modelled with a fixed rate, i.e. the probability of the synapse failing for a received spike is given as the failure rate in Supplementary Table 3.

Thalamic Inputs Into the Barrel Cortex in Silico

To the best of our knowledge, there is not any published quantitative work on the cellular organization of the mouse thalamic nuclei. In the rat, each barreloid in thalamic VPM nuclei has ~ 1/18 number of neurons compared to the corresponding L4 barrel (Meyer et al., 2013). Given that in our average barrel column L4 contains ~ 1600 neurons, we assigned between 100 and 200 thalamic neurons to each barreloid in VPM. The thalamic-cortical connectivity is calculated using the same method as cortical-cortical connectivity discussed above, using published thalamic axon projection patterns (Furuta et al., 2011; Oberlaender et al., 2012). The POM pathway was not modeled.

Each of the thalamic neurons is modelled as a 'filter and fire' neuron (Chichilnisky, 2001; Keat et al., 2001; Pillow et al., 2008; Truccolo et al., 2005), where each of the thalamic neurons responds to either whisker angle (filters and activation functions randomly chosen based on a parametrization of the filters from (Petersen et al., 2008)), curvature, or a combination of both. The center barreloid was considered to be the principal barreloid for the spared whisker, whereas the other two were considered secondary barreloids, which meant that they received the stimuli reduced (30% of original amplitude) and delayed (2.5 ms) (Brecht & Sakmann, 2002; Brecht et al., 2003). The thalamic spike trains served as input to the cortical model, which similarly consisted of three cortical columns, corresponding to the three thalamic barreloids.

Thalamic stimulation in the model based on population PSTHs (Figs. 2–7) was collected extracellularly in anesthetized animals in *vivo* (Aguilar & Castro-Alamancos, 2005). The PSTHs only specified the population firing rate in the thalamic cells; to generate individual neuron response in different trials we assume that thalamic neurons fire independent Poisson spike trains in each trial, constrained by the PSTHs.

Spike-Timing Dependent Plasticity

A network of 3 barrel columns, representing canonical C,D,E rows, was constructed to simulate pairwise spike-timing-dependent plasticity in the barrel cortex following a single (D-row) whisker deprivation. Each column was randomly generated using distributions of 13 different types of neurons, and connectivity was calculated using the same method discussed above. The middle column was whisker-deprived, which received surround whisker evoked thalamic input; the two lateral columns were whisker-spared and received principal whisker evoked thalamic input (Aguilar & Castro-Alamancos, 2005). The pairwise STDP rule for L4-L2/3 excitatory connections was as follows (Celikel et al., 2004):

$$dA = \begin{cases} -3.7 \cdot 10^6 (\Delta t)^2 - 0.0019\Delta t + 0.77 & \text{if } -250 \le \Delta t \le 0 \\ \frac{0.5665\Delta t}{3} - 0.23 & \text{if } 0 < \Delta t \le 3 \\ -4.7 \cdot 10^{-7} (\Delta t)^3 - 0.00028(\Delta t)^2 - 0.022\Delta t + 1.4 & \text{if } 3 \le \Delta t \le 32 \end{cases}$$

Δt was the timing difference (in ms) between the time at which a presynaptic spike arrives at a postsynaptic neuron (i.e. the presynaptic neuron's spike time plus synaptic delay) and the time at which the postsynaptic neuron spikes in ms. The constants were directly taken from the literature, in which the values were obtained by least-square fits to the experimental data. For L2/3-L2/3 excitatory connections, the rule was as follows (Banerjee et al., 2014):

$$dA = \begin{cases} \frac{0.53}{100} e^{\frac{-\Delta t}{18}} & \text{if } \Delta t \ge 0 \\ -\frac{0.32}{100} e^{\frac{-\Delta t}{18}} & \text{if } \Delta t < 0 \end{cases}$$

The synaptic weight change was additive ($A_{new} = A_{old} + dA$) for potentiation and multiplicative ($A_{new} = A_{old}(1 - dA)$ for depression; repeating the simulations with an additive rule for potentiation and depression did not change the results and are not shown herein. Plasticity rules for excitatory-inhibitory and inhibitory connections are less commonly studied. Inclusion of the empirically identified learning curves (Haas et al., 2006; Lu et al., 2007) did not qualitatively alter the results and are not included herein.

Simulated Freely Whisking Experiment

In the simulations of a freely whisking experiment, the network (Fig. 8: 3 barrels, Fig. 9: 1 barrel) was presented with the whisker angle and curvature recorded from a freely whisking rat (animal an171923, session 2012_06_04) in a pole localization task (data from (Peron et al., 2015) made available as 'ssc-2' on CRCNS.org).

NB Direct whisker modulation by motor cortex (Crochet et al., 2011) can be optionally included in the model, but was not used for our current simulations. However, it is present in the online code as option.

The calculation of the fluorescence from the spike train data wat calculated with the help of the model by (Vogelstein et al., 2009):

$$[C]\left(t + \Delta t_C\right) = [C](t) + \Delta[C]$$

$$\Delta[C] = -\frac{\Delta t_C}{\tau_C}\left([C] - [C]_b\right) + A_c\left(N_{spikes\,in\,bin}\right) + \sigma_C\sqrt{\Delta t_C}\eta_C$$

$$L\left(t + \Delta t_C\right) = L(t) + \Delta L$$

$$\Delta L = \alpha[C]\left(t + \Delta t_C\right) + \beta + \sigma_f \eta_f.$$

The calcium concentration $[C]$ (a.u.) is calculated at a lower sampling frequency (7 Hz, resulting in $\Delta t_C = \frac{1000}{7} \approx 143$ ms) than the model calculations, like in the recordings. It decays exponentially (time constant $\tau_C = 500$ ms) to baseline $[C]_b = 0.1$ (a.u.) and is increased with amount $A_c = 5$ (a.u.) for each spike with additive Gaussian noise with standard deviation $\sigma_C = 1$ (a.u.). The luminescence L (a.u.) is a linear function of the calcium concentration, with scaling $\alpha = 1$, offset $\beta = 0$ and additive Gaussian noise with standard deviation $\sigma_f = 1$.

NetPyNE Implementation

To allow for simulations in other platforms, including Brian (Stimberg et al., 2019), NEST (Gewaltig & Diesmann, 2007) and NEURON (Carnevale & Hines, 2006), we have added a NetPyNE (Dura-Bernal et al., 2019) implementation of the model with the help of MetaCell LLC Ltd and the Dura-Bernal Lab at SUNY Downstate. This implementation allows for exportation to many platforms, including the ones mentioned above, through NeuroML and SONATA (Gleeson et al., 2010). Also, using this implementation network properties can easily be adapted (i.e. replace Izhikevich neurons (Izhikevich, 2003, 2004) by adaptive exponential IF neurons (Brette & Gerstner, 2005)) or Hodgkin-Huxley multicompartment neurons. This implementation can be found in the GitHub repository mentioned at the start of this section. Note that there are a few small differences between the MatLab and the NetPyNE implementations:

1. Because in NetPyNE and NEURON synapses require separate objects ('NetCons') and a synaptic mechanisms such as 'Exp2syn', the NetPyNE implementation is computationally heavier than the Matlab implementation. So the NetPyNE implementation might require a high-performance computing (HPC) cluster. Our test simulations were run were run on cloud-based HPC clusters, more specifically, Google Cloud. The event-based nature of the model in NetPyNE makes it easier to run it in parallel though.
2. Because NetPyNE uses a different (event-based backward Euler method) solver (instead of forward Euler in the Matlab version), and initial conditions are naturally on steady states rather than at fixed settings, there might be small differences in individual spike timings, and because these systems are close to chaos, these differences become larger over time. However, overall conclusions should not be different.
3. In NetPyNE, the creation of connectivity based on the measured distribution of overlapping axon and dendrites, as described above, is currently not possible: NetPyNE does allow to create connectivity based on distributions of other properties. Therefore, we have added a few realisations to the following data repository: https://doi.org/10.34973/tmf3-2m63 These can be loaded into the NetPyNE model.

Supplementary Information The online version contains supplementary material available at https://doi.org/10.1007/s12021-022-09576-5.

Acknowledgements The authors would like to thank Matteo Cantarelli of MetaCell LLC Ltd, and Salvador Dura-Bernal and Eugenio Urdapilleta of the Dura-Bernal Lab, SUNY Downstate for the conversion of the model to NetPyNE.

Funding This work was supported by grants from the European Commission (Horizon2020, nr. 660328), European Regional Development Fund (MIND, nr. 122035) and the Netherlands Organisation for Scientific Research (NWO-ALW Open Competition, nr. 824.14.022) to TC and by the Netherlands Organisation for Scientific Research (NWO Veni Research Grant, nr. 863.150.25) to FZ.

Availability of Data and Material All data are in the model, and therefore in the code.

Code Availability All code can be found in the following repositories: https://github.com/DepartmentofNeurophysiology/Cortical-representation-of-touch-in-silico. https://github.com/DepartmentofNeurophysiology/Cortical-representation-of-touch-in-silico-NetPyne. A few connectivity realizations can be found here: https://doi.org/10.34973/tmf3-2m63

Declarations

Ethical Approval All experimental procedures were performed according to Dutch law and approved by the Ethical Committee for Animal Experimentation of Radboud University (RU DEC).

Conflicts of Interest/Competing Interests The authors declare that no competing interests exist.

References

Aguilar, J. R., & Castro-Alamancos, M. A. (2005). Spatiotemporal Gating of Sensory Inputs in Thalamus during Quiescent and Activated States. *Journal of Neuroscience, 25*(47), 10990–11002. https://doi.org/10.1523/JNEUROSCI.3229-05.2005

Allen, C. B., Celikel, T., & Feldman, D. E. (2003). Long-term depression induced by sensory deprivation during cortical map plasticity in vivo. *Nature Neuroscience, 6*(3), 291–299. https://doi.org/10.1038/nn1012

Ananthanarayanan, R., Esser, S. K., Simon, H. D., & Modha, D. S. (2009). The cat is out of the bag. *Proceedings of the Conference on High Performance Computing Networking, Storage and Analysis - SC '09*, 1. https://doi.org/10.1145/1654059.1654124

Arkhipov, A., Gouwens, N. W., Billeh, Y. N., Gratiy, S., Iyer, R., Wei, Z., Xu, Z., Abbasi-Asl, R., Berg, J., Buice, M., Cain, N., da Costa, N., de Vries, S., Denman, D., Durand, S., Feng, D., Jarsky, T., Lecoq, J., Lee, B., & Koch, C. (2018). Visual physiology of the layer 4 cortical circuit in silico. *PLOS Computational Biology, 14*(11), e1006535. https://doi.org/10.1371/journal.pcbi.1006535

Armstrong-James, M., & Callahan, C. A. (1991). Thalamo-cortical processing of vibrissal information in the rat. II. Spatiotemporal convergence in the thalamic ventroposterior medial nucleus (VPm) and its relevance to generation of receptive fields of S1 cortical "Barrel" neurones. *Journal of Comparative Neurology*, *303*(2), 211–224. https://doi.org/10.1002/cne.903030204

Armstrong-James, M., Fox, K., & Das-Gupta, A. (1992). Flow of excitation within rat barrel cortex on striking a single vibrissa. *Journal of Neurophysiology, 68*(4), 1345–1358. https://doi.org/10.1152/jn.1992.68.4.1345

Arnold, P. B., Li, C. X., & Waters, R. S. (2001). Thalamocortical arbors extend beyond single cortical barrels: An in vivo intracellular tracing study in rat. *Experimental Brain Research, 136*(2), 152–168. https://doi.org/10.1007/s002210000570

Azarfar, A., Calcini, N., Huang, C., Zeldenrust, F., & Celikel, T. (2018a). Neural coding: A single neuron's perspective. *Neuroscience & Biobehavioral Reviews, 94*, 238–247. https://doi.org/10.1016/j.neubiorev.2018.09.007

Azarfar, A., Zhang, Y., Alishbayli, A., Miceli, S., Kepser, L., van der Wielen, D., van de Moosdijk, M., Homberg, J., Schubert, D., Proville, R., & Celikel, T. (2018b). An open-source high-speed infrared videography database to study the principles of active sensing in freely navigating rodents. *GigaScience*, *7*(12). https://doi.org/10.1093/gigascience/giy134

Badel, L., Lefort, S., Brette, R., Petersen, C. C. H., Gerstner, W., & Richardson, M. J. E. (2008). Dynamic I-V Curves Are Reliable Predictors of Naturalistic Pyramidal-Neuron Voltage Traces. *Journal of Neurophysiology, 99*, 656–666.

Banerjee, A., González-Rueda, A., Sampaio-Baptista, C., Paulsen, O., & Rodríguez-Moreno, A. (2014). Distinct mechanisms of spike timing-dependent LTD at vertical and horizontal inputs onto L2/3 pyramidal neurons in mouse barrel cortex. *Physiological Reports, 2*(3), e00271. https://doi.org/10.1002/phy2.271

Bassett, D. S., & Bullmore, E. (2006). Small-World Brain Networks. *The Neuroscientist, 12*(6), 512–523. https://doi.org/10.1177/1073858406293182

Beierlein, M., Gibson, J. R., & Connors, B. W. (2003). Two Dynamically Distinct Inhibitory Networks in Layer 4 of the Neocortex. *Journal of Neurophysiology, 90*(5), 2987–3000. https://doi.org/10.1152/jn.00283.2003

Bender, K. J., Allen, C. B., Bender, V. A., & Feldman, D. E. (2006). Synaptic Basis for Whisker Deprivation-Induced Synaptic Depression in Rat Somatosensory Cortex. *Journal of Neuroscience, 26*(16), 4155–4165. https://doi.org/10.1523/JNEUROSCI.0175-06.2006

Bernardi, D., Doron, G., Brecht, M., & Lindner, B. (2021). A network model of the barrel cortex combined with a differentiator detector reproduces features of the behavioral response to single-neuron stimulation. *PLOS Computational Biology, 17*(2), e1007831. https://doi.org/10.1371/journal.pcbi.1007831

Billeh, Y. N., Cai, B., Gratiy, S. L., Dai, K, Iyer, R., Gouwens, N. W., Abbasi-Asl, R., Jia, X., Siegle, J. H., Olsen, S. R., Koch, C., Mihalas, S., & Arkhipov, A. (2019). Systematic integration of structural and functional data into multi-scale models of mouse primary visual cortex. *BioRxiv,* 662189. https://doi.org/10.1101/662189

Blatow, M., Rozov, A., Katona, I., Hormuzdi, S. G., Meyer, A. H., Whittington, M. A., Caputi, A., & Monyer, H. (2003). A Novel Network of Multipolar Bursting Interneurons Generates Theta Frequency Oscillations in Neocortex. *Neuron, 38*(5), 805–817. https://doi.org/10.1016/S0896-6273(03)00300-3

Botella-Soler, V., Deny, S., Martius, G., Marre, O., & Tkačik, G. (2018). Nonlinear decoding of a complex movie from the mammalian retina. *PLOS Computational Biology, 14*(5), e1006057. https://doi.org/10.1371/journal.pcbi.1006057

Brecht, M., Roth, A., & Sakmann, B. (2003). Dynamic receptive fields of reconstructed pyramidal cells in layers 3 and 2 of rat somatosensory barrel cortex. *The Journal of Physiology, 553*, 243–265. https://doi.org/10.1113/jphysiol.2003.044222

Brecht, M., & Sakmann, B. (2002). Dynamic representation of whisker deflection by synaptic potentials in spiny stellate and pyramidal cells in the barrels and septa of layer 4 rat somatosensory cortex. *The Journal of Physiology, 543*(Pt 1), 49–70. https://doi.org/10.1113/jphysiol.2002.018465

Brette, R., & Gerstner, W. (2005). Adaptive exponential integrate-and-fire model as an effective description of neuronal activity. *Journal of Neurophysiology, 94*(5), 3637–3642. https://doi.org/10.1152/jn.00686.2005

Brunel, N. (2000). Dynamics of Sparsely Connected Networks of Excitatory and Inhibitory Spiking Neurons. *Journal of Computational Neuroscience*, *8*.

Caputi, A., Rozov, A., Blatow, M., & Monyer, H. (2009). Two calretinin-positive GABAergic cell types in layer 2/3 of the mouse neocortex provide different forms of inhibition. *Cerebral Cortex (New York, N.Y.: 1991)*, *19*(6), 1345–1359. https://doi.org/10.1093/cercor/bhn175

Carnevale, T., & Hines, M. (2006). *The NEURON book*. Cambridge University Press.

Celikel, T., Szostak, V. A., & Feldman, D. E. (2004). Modulation of spike timing by sensory deprivation during induction of cortical map plasticity. *Nature Neuroscience, 7*(5), 534–541. https://doi.org/10.1038/nn1222

Chariker, L., Shapley, R., & Young, L. S. (2016). Orientation selectivity from very sparse LGN inputs in a comprehensive model of macaque V1 cortex. *Journal of Neuroscience, 36*(49), 12368–12384. https://doi.org/10.1523/JNEUROSCI.2603-16.2016

Chichilnisky, E. J. (2001). A simple white noise analysis of neuronal light responses. *Network: Computation in Neural Systems*, *12*, 199–213.

Chu, Y., Fei, J., & Hou, S. (2020). Adaptive Global Sliding-Mode Control for Dynamic Systems Using Double Hidden Layer Recurrent Neural Network Structure. *IEEE Transactions on Neural Networks and Learning Systems, 31*(4), 1297–1309. https://doi.org/10.1109/TNNLS.2019.2919676

Clem, R. L., Celikel, T., & Barth, A. L. (2008). Ongoing in vivo experience triggers synaptic metaplasticity in the neocortex. *Science, 319*(5859), 101–104. https://doi.org/10.1126/science.1143808

Condylis, C., Lowet, E., Ni, J., Bistrong, K., Ouellette, T., Josephs, N., & Chen, J. L. (2020). Context-Dependent Sensory Processing across Primary and Secondary Somatosensory Cortex. *Neuron, 106*(3), 515-525.e5. https://doi.org/10.1016/j.neuron.2020.02.004

Crochet, S., Poulet, J. F. A., Kremer, Y., & Petersen, C. C. H. (2011). Synaptic Mechanisms Underlying Sparse Coding of Active Touch. *Neuron, 69*(6), 1160–1175. https://doi.org/10.1016/j.neuron.2011.02.022

da Silva Lantyer, A., Calcini, N., Bijlsma, A., Kole, K., Emmelkamp, M., Peeters, M., Scheenen, W. J. J., Zeldenrust, F., & Celikel, T. (2018). A databank for intracellular electrophysiological mapping of the adult somatosensory cortex. *GigaScience, 7*(12), 1–9. https://doi.org/10.1093/gigascience/giy147

De Kock, C. P. J., Bruno, R. M., Spors, H., & Sakmann, B. (2007). Layer- and cell-type-specific suprathreshold stimulus representation in rat primary somatosensory cortex. *The Journal of Physiology, 581*(1), 139–154. https://doi.org/10.1113/jphysiol.2006.124321

Denk, W., & Detwiler, P. B. (1999). Optical recording of light-evoked calcium signals in the functionally intact retina. *Proceedings of the National Academy of Sciences, 96*(12), 7035–7040. https://doi.org/10.1073/pnas.96.12.7035

Diamond, M. E., Armstrong-James, M., & Ebner, F. F. (1992). Somatic sensory responses in the rostral sector of the posterior group (POm) and in the ventral posterior medial nucleus (VPM) of the rat thalamus. *Journal of Comparative Neurology, 318*(4), 462–476. https://doi.org/10.1002/cne.903180410

Doi, E., Gauthier, J. L., Field, G. D., Shlens, J., Sher, A., Greschner, M., Machado, T., & a, Jepson, L. H., Mathieson, K., Gunning, D. E., Litke, A. M., Paninski, L., Chichilnisky, E. J., & Simoncelli, E. P. (2012). Efficient coding of spatial information in the primate retina. *The Journal of Neuroscience, 32*(46), 16256–16264. https://doi.org/10.1523/JNEUROSCI.4036-12.2012

Douglas, R. J., & Martin, K. A. C. (2004). Neuronal circuits of the neocortex. *Annual Review of Neuroscience, 27*, 419–451. https://doi.org/10.1146/annurev.neuro.27.070203.144152

Douglas, R. J., & Martin, K. A. C. (2007). Recurrent neuronal circuits in the neocortex. *Current Biology, 17*(13), R496–R500. https://doi.org/10.1016/j.cub.2007.04.024

Dudai, A., Yayon, N., Lerner, V., Tasaka, G., Deitcher, Y., Gorfine, K., Niederhoffer, N., Mizrahi, A., Soreq, H., & London, M. (2020). Barrel cortex VIP/ChAT interneurons suppress sensory responses in vivo. *PLOS Biology, 18*(2), e3000613. https://doi.org/10.1371/journal.pbio.3000613

Dura-Bernal, S., Suter, B. A., Gleeson, P., Cantarelli, M., Quintana, A., Rodriguez, F., Kedziora, D. J., Chadderdon, G. L., Kerr, C. C., Neymotin, S. A., McDougal, R. A., Hines, M., Shepherd, G. M., & Lytton, W. W. (2019). NetPyNE, a tool for data-driven multiscale modeling of brain circuits. *eLife, 8*, e44494. https://doi.org/10.7554/eLife.44494

Edelman, G. M., & Gally, J. (2001). Degeneracy and Complexity in Biological Systems. *Proceedings of the National Academy of Sciences, 98*(24), 13763–13768.

Egger, V., Nevian, T., & Bruno, R. M. (2008). Subcolumnar Dendritic and Axonal Organization of Spiny Stellate and Star Pyramid Neurons within a Barrel in Rat Somatosensory Cortex. *Cerebral Cortex, 18*(4), 876–889. https://doi.org/10.1093/cercor/bhm126

Einevoll, G. T., Destexhe, A., Diesmann, M., Grün, S., Jirsa, V., de Kamps, M., Migliore, M., Ness, T. V., Plesser, H. E., & Schürmann, F. (2019). The Scientific Case for Brain Simulations. *Neuron, 102*(4), 735–744. https://doi.org/10.1016/j.neuron.2019.03.027

Eliasmith, C., & Trujillo, O. (2014). The use and abuse of large-scale brain models. *Current Opinion in Neurobiology, 25*, 1–6. https://doi.org/10.1016/j.conb.2013.09.009

Fan, X., & Markram, H. (2019). A Brief History of Simulation Neuroscience. *Frontiers in Neuroinformatics, 13*, 32. https://doi.org/10.3389/fninf.2019.00032

Feldman, D. E., & Brecht, M. (2005). Map plasticity in somatosensory cortex. *Science, 310*(5749), 810–815. https://doi.org/10.1126/science.1115807

Feldmeyer, D., Lübke, J., & Sakmann, B. (2006). Efficacy and connectivity of intracolumnar pairs of layer 2/3 pyramidal cells in the barrel cortex of juvenile rats: Layer 2/3 pyramidal cell synapses. *The Journal of Physiology, 575*(2), 583–602. https://doi.org/10.1113/jphysiol.2006.105106

Feldmeyer, D., Lübke, J., Silver, R. A., & Sakmann, B. (2002). Synaptic connections between layer 4 spiny neurone- layer 2/3 pyramidal cell pairs in juvenile rat barrel cortex: Physiology and anatomy of interlaminar signalling within a cortical column. *The Journal of Physiology, 538*(Pt 3), 803. https://doi.org/10.1113/jphysiol.2001.012959

Field, G. D., & Chichilnisky, E. J. (2007). Information Processing in the Primate Retina: Circuitry and Coding. *Annual Review of Neuroscience, 30*(1), 1–30. https://doi.org/10.1146/annurev.neuro.30.051606.094252

Fino, E., & Yuste, R. (2011). Dense inhibitory connectivity in neocortex. *Neuron, 69*(6), 1188–1203. https://doi.org/10.1016/j.neuron.2011.02.025

Foeller, E., Celikel, T., & Feldman, D. E. (2005). Inhibitory sharpening of receptive fields contributes to whisker map plasticity in rat somatosensory cortex. *Journal of Neurophysiology, 94*, 4387–4400. https://doi.org/10.1152/jn.00553.2005

Fontaine, B., Peña, J. L., & Brette, R. (2014). Spike-Threshold Adaptation Predicted by Membrane Potential Dynamics In Vivo. *PLoS Computational Biology, 10*(4), 1–11. https://doi.org/10.1371/journal.pcbi.1003560

Fox, K. (2018). Deconstructing the Cortical Column in the Barrel Cortex. *Neuroscience, 368*, 17–28. https://doi.org/10.1016/j.neuroscience.2017.07.034

Furuta, T., Deschênes, M., & Kaneko, T. (2011). Anisotropic Distribution of Thalamocortical Boutons in Barrels. *Journal of Neuroscience, 31*(17), 6432–6439. https://doi.org/10.1523/JNEUROSCI.6154-10.2011

Gentet, L. J., Avermann, M., Matyas, F., Staiger, J. F., & Petersen, C. C. H. (2010). Membrane Potential Dynamics of GABAergic Neurons in the Barrel Cortex of Behaving Mice. *Neuron, 65*(3), 422–435. https://doi.org/10.1016/j.neuron.2010.01.006

Gentet, L. J., Kremer, Y., Taniguchi, H., Huang, Z. J., Staiger, J. F., & Petersen, C. C. H. (2012). Unique functional properties of somatostatin-expressing GABAergic neurons in mouse barrel cortex. *Nature Neuroscience, 15*(4), 607–612. https://doi.org/10.1038/nn.3051

Gerstner, W., & Kistler, W. M. (2002). *Spiking Neuron Models: Single Neurons, Populations, Plasticity*. Cambridge University Press. https://lcnwww.epfl.ch/gerstner/SPNM/SPNM.html

Gerstner, W., & Naud, R. (2009). How good are neuron models? *Science, 326*(5951), 379–380. https://doi.org/10.1126/science.1181936

Gewaltig, M. O., & Diesmann, M. (2007). NEST (NEural Simulation Tool). *Scholarpedia, 2*(4), 1430.

Gibson, J. R., Beierlein, M., & Connors, B. W. (1999). Two networks of electrically coupled inhibitory neurons in neocortex. *Nature, 402*(6757), 75–79. https://doi.org/10.1038/47035

Gleeson, P., Crook, S., Cannon, R. C., Hines, M. L., Billings, G. O., Farinella, M., Morse, T. M., Davison, A. P., Ray, S., Bhalla, U. S., Barnes, S. R., Dimitrova, Y. D., & Silver, R. A. (2010). NeuroML: A language for describing data driven models of neurons and networks with a high degree of biological detail. *PLoS Computational Biology, 6*(6), 1–19. https://doi.org/10.1371/journal.pcbi.1000815

Guizar-Sicairos, M., Thurman, S. T., & Fienup, J. R. (2008). Efficient subpixel image registration algorithms. *Optics Letters, 33*(2), 156–158.

Gutkin, B. S., & Ermentrout, G. B. (2006). Spikes too kinky in the cortex ? *Nature*, *440*(April).

Haas, J. S., Nowotny, T., & Abarbanel, H. D. I. (2006). Spike-timing-dependent plasticity of inhibitory synapses in the entorhinal cortex. *Journal of Neurophysiology, 96*(6), 3305–3313. https://doi.org/10.1152/jn.00551.2006

Hardingham, N. R., Gould, T., & Fox, K. (2011). Anatomical and sensory experiential determinants of synaptic plasticity in layer 2/3 pyramidal neurons of mouse barrel cortex. *Journal of Comparative Neurology, 519*(11), 2090–2124. https://doi.org/10.1002/cne.22583

Harrison, P. M., Badel, L., Wall, M. J., & Richardson, M. J. E. (2015). Experimentally Verified Parameter Sets for Modelling Heterogeneous Neocortical Pyramidal-Cell Populations. *PLOS Computational Biology, 11*(8), e1004165. https://doi.org/10.1371/journal.pcbi.1004165

Heckbert, P. S. (Ed.). (1994). *Graphics Gems IV* (Vol. 4). Academic Press Professional, Inc.

Helmstaedter, M., Briggman, K. L., Turaga, S. C., Jain, V., Seung, H. S., & Denk, W. (2013). Connectomic reconstruction of the inner plexiform layer in the mouse retina. *Nature, 500*(7461), 168–174. https://doi.org/10.1038/nature12346

Helmstaedter, M., Staiger, J. F., Sakmann, B., & Feldmeyer, D. (2008). Efficient Recruitment of Layer 2/3 Interneurons by Layer 4 Input in Single Columns of Rat Somatosensory Cortex. *Journal of Neuroscience, 28*(33), 8273–8284. https://doi.org/10.1523/JNEUROSCI.5701-07.2008

Hodge, R. D., D'Ercole, A. J., & O'Kusky, J. R. (2005). Increased expression of insulin-like growth factor-I (IGF-I) during embryonic development produces neocortical overgrowth with differentially greater effects on specific cytoarchitectonic areas and cortical layers. *Developmental Brain Research, 154*(2), 227–237. https://doi.org/10.1016/j.devbrainres.2004.10.016

Holmgren, C., Harkany, T., Svennenfors, B., & Zilberter, Y. (2003). Pyramidal cell communication within local networks in layer 2/3 of rat neocortex. *The Journal of Physiology, 551*(1), 139–153. https://doi.org/10.1113/jphysiol.2003.044784

Hopfield, J. J. (1982). Neural networks and physical systems with emergent collective computational abilities. *Proceedings of the National Academy of Sciences, 79*, 2554–2558.

Huang, C., Englitz, B., Reznik, A., Zeldenrust, F., & Celikel, T. (2020). Information transfer and recovery for the sense of touch. *BioRxiv*. https://doi.org/10.1101/2020.12.08.415729

Huang, C., Resnik, A., Celikel, T., & Englitz, B. (2016). Adaptive Spike Threshold Enables Robust and Temporally Precise Neuronal Encoding. *PLoS Computational Biology, 12*(6), e1004984. https://doi.org/10.1371/journal.pcbi.1004984

Irintchev, A., Rollenhagen, A., Troncoso, E., Kiss, J. Z., & Schachner, M. (2005). Structural and Functional Aberrations in the Cerebral Cortex of Tenascin-C Deficient Mice. *Cerebral Cortex, 15*(7), 950–962. https://doi.org/10.1093/cercor/bhh195

Izhikevich, E. M. (2003). Simple Model of Spiking Neurons. *IEEE Transactions on Neural Networks, 14*(6), 1572–1596. https://doi.org/10.1109/TNN.2003.820440

Izhikevich, E. M. (2004). Which model to use for cortical spiking neurons? *IEEE Transactions on Neural Networks, 15*(5), 1063–1070.

Izhikevich, E. M., & Edelman, G. M. (2008). Large-scale model of mammalian thalamocortical systems. *Proceedings of the National Academy of Sciences, 105*(9), 3593–3598.

Jolivet, R., Lewis, T. J., & Gerstner, W. (2004). Generalized integrate-and-fire models of neuronal activity approximate spike trains of a detailed model to a high degree of accuracy. *Journal of Neurophysiology, 92*(2), 959–976. https://doi.org/10.1152/jn.00190.2004

Jones, D. L., Johnson, E. C., & Ratnam, R. (2015). A stimulus-dependent spike threshold is an optimal neural coder. *Frontiers in Computational Neuroscience, 9*. https://doi.org/10.3389/fncom.2015.00061

Kapfer, C., Glickfeld, L. L., Atallah, B. V., & Scanziani, M. (2007). Supralinear increase of recurrent inhibition during sparse activity in the somatosensory cortex. *Nature Neuroscience, 10*(6), 743–753. https://doi.org/10.1038/nn1909

Kato, S., Kaplan, H. S., Yemini, E., Zimmer, M., Skora, S., Lindsay, T. H., Yemini, E., Lockery, S., & Zimmer, M. (2015). Global brain dynamics embed the motor command sequence of caenorhabditis elegans. *Cell*, 1–14 https://doi.org/10.1016/j.cell.2015.09.034

Kawaguchi, Y., & Kubota, Y. (1997). GABAergic cell subtypes and their synaptic connections in rat frontal cortex. *Cerebral Cortex, 7*(6), 476–486. https://doi.org/10.1093/cercor/7.6.476

Keat, J., Reinagel, P., Clay Reid, R., & Meister, M. (2001). Predicting Every Spike: A Model for the Responses of Visual Neurons. *Neuron, 30*, 803–817.

Kerr, J. N. D., de Kock, C. P. J., Greenberg, D. S., Bruno, R. M., Sakmann, B., & Helmchen, F. (2007). Spatial Organization of Neuronal Population Responses in Layer 2/3 of Rat Barrel Cortex. *Journal of Neuroscience, 27*(48), 13316–13328. https://doi.org/10.1523/JNEUROSCI.2210-07.2007

Kobayashi, R., Tsubo, Y., & Shinomoto, S. (2009). Made-to-order spiking neuron model equipped with a multi-timescale adaptive threshold. *Frontiers in Computational Neuroscience, 3*(July), 9. https://doi.org/10.3389/neuro.10.009.2009

Koelbl, C., Helmstaedter, M., Lübke, J., & Feldmeyer, D. (2015). A Barrel-Related Interneuron in Layer 4 of Rat Somatosensory Cortex with a High Intrabarrel Connectivity. *Cerebral Cortex, 25*(3), 713–725. https://doi.org/10.1093/cercor/bht263

Kole, K., & Celikel, T. (2019). Neocortical Microdissection at Columnar and Laminar Resolution for Molecular Interrogation. *Current Protocols in Neuroscience, 86*(1), e55. https://doi.org/10.1002/cpns.55

Kole, K., Komuro, Y., Provaznik, J., Pistolic, J., Benes, V., Tiesinga, P., & Celikel, T. (2017). Transcriptional mapping of the primary somatosensory cortex upon sensory deprivation. *GigaScience, 6*, 1–6. https://doi.org/10.1093/gigascience/gix081

Kole, K., Lindeboom, R. G. H., Baltissen, M. P. A., Jansen, P. W. T. C., Vermeulen, M., Tiesinga, P., & Celikel, T. (2018). Proteomic landscape of the primary somatosensory cortex upon sensory deprivation. *GigaScience, 6*, 1–10. https://doi.org/10.1093/gigascience/gix082

Kole, K., Scheenen, W., Tiesinga, P., & Celikel, T. (2018). Cellular diversity of the somatosensory cortical map plasticity. *Neuroscience & Biobehavioral Reviews, 84*, 100–115. https://doi.org/10.1016/j.neubiorev.2017.11.015

Kole, K., Zhang, Y., Jansen, E. J. R., Brouns, T., Bijlsma, A., Calcini, N., Yan, X., da Lantyer, A., & S., & Celikel, T. (2020). Assessing the utility of Magneto to control neuronal excitability in the somatosensory cortex. *Nature Neuroscience, 23*(9), 1044–1046. https://doi.org/10.1038/s41593-019-0474-4

Kole, M. H. P., & Brette, R. (2018). The electrical significance of axon location diversity. *Current Opinion in Neurobiology, 51*, 52–59. https://doi.org/10.1016/j.conb.2018.02.016

Kwegyir-Afful, E. E., Bruno, R. M., Simons, D. J., & Keller, A. (2005). The Role of Thalamic Inputs in Surround Receptive Fields of Barrel Neurons. *Journal of Neuroscience, 25*(25), 5926–5934. https://doi.org/10.1523/JNEUROSCI.1360-05.2005

Landau, I. D., Egger, R., Dercksen, V. J., Oberlaender, M., & Sompolinsky, H. (2016). The Impact of Structural Heterogeneity on Excitation-Inhibition Balance in Cortical Networks. *Neuron, 92*(5), 1106–1121. https://doi.org/10.1016/j.neuron.2016.10.027

Li, P. H., Gauthier, J. L., Schiff, M., Sher, A., Ahn, D., Field, G. D., Greschner, M., Callaway, E. M., Litke, A. M., & Chichilnisky, E. J. (2015). Anatomical Identification of Extracellularly Recorded Cells in Large-Scale Multielectrode Recordings. *The Journal of Neuroscience, 35*(11), 4663–4675. https://doi.org/10.1523/JNEUROSCI.3675-14.2015

Lu, J., Li, C., Zhao, J.-P., Poo, M., & Zhang, X. (2007). Spike-Timing-Dependent Plasticity of Neocortical Excitatory Synapses on Inhibitory Interneurons Depends on Target Cell Type. *Journal of Neuroscience, 27*(36), 9711–9720. https://doi.org/10.1523/JNEUROSCI.2513-07.2007

Lübke, J., Roth, A., Feldmeyer, D., & Sakmann, B. (2003). Morphometric Analysis of the Columnar Innervation Domain of Neurons Connecting Layer 4 and Layer 2/3 of Juvenile Rat Barrel Cortex. *Cerebral Cortex, 13*(10), 1051–1063. https://doi.org/10.1093/cercor/13.10.1051

Lyck, L., Krøigård, T., & Finsen, B. (2007). Unbiased cell quantification reveals a continued increase in the number of neocortical neurones during early post-natal development in mice. *European Journal of Neuroscience, 26*(7), 1749–1764. https://doi.org/10.1111/j.1460-9568.2007.05763.x

Ma, D., Descarries, L., Micheva, K. D., Lepage, Y., Julien, J.-P., & Doucet, G. (1999). Severe neuronal losses with age in the parietal cortex and ventrobasal thalamus of mice transgenic for the human NF-L neurofilament protein. *Journal of Comparative Neurology, 406*(4), 433–448. https://doi.org/10.1002/(SICI)1096-9861(19990419)406:4%3c433::AID-CNE2%3e3.0.CO;2-3

Marder, E., & Goaillard, J.-M. (2006). Variability, compensation and homeostasis in neuron and network function. *Nature Reviews, 7*(July), 563–574. https://doi.org/10.1038/nrn1949

Marder, E., & Taylor, A. L. (2011). Multiple models to capture the variability in biological neurons and networks. *Nature Neuroscience, 14*(2), 133–138. https://doi.org/10.1038/nn.2735

Markram, H. (2006). The blue brain project. *Nature Reviews. Neuroscience, 7*(2), 153–160. https://doi.org/10.1038/nrn1848

Markram, H., Muller, E., Ramaswamy, S., Reimann, M. W., Abdellah, M., Sanchez, C. A., Ailamaki, A., Alonso-Nanclares, L., Antille, N., Arsever, S., Kahou, G. A. A., Berger, T. K., Bilgili, A., Buncic, N., Chalimourda, A., Chindemi, G., Courcol, J.-D., Delalondre, F., Delattre, V., & Schürmann, F. (2015). Reconstruction and Simulation of Neocortical Microcircuitry. *Cell, 163*(2), 456–492. https://doi.org/10.1016/j.cell.2015.09.029

Markram, H., Toledo-rodriguez, M., Wang, Y., Gupta, A., Silberberg, G., & Wu, C. (2004). Interneurons of the Neocortical Inhibitory System. *Nature Reviews. Neuroscience, 5*, 793–807. https://doi.org/10.1038/nrn1519

Marre, O., Amodei, D., Deshmukh, N., Sadeghi, K., Soo, F., Holy, T. E., & Berry, M. J. (2012). Mapping a complete neural population in the retina. *The Journal of Neuroscience, 32*(43), 14859–14873. https://doi.org/10.1523/JNEUROSCI.0723-12.2012

Meyer, F. (1994). Topographic distance and watershed lines. *Signal Processing, 38*(1), 113–125. https://doi.org/10.1016/0165-1684(94)90060-4

Meyer, H. S., Egger, R., Guest, J. M., Foerster, R., Reissl, S., & Oberlaender, M. (2013). Cellular organization of cortical barrel columns is whisker-specific. *Proceedings of the National Academy of Sciences of the United States of America, 110*(47), 19113–19118. https://doi.org/10.1073/pnas.1312691110

Meyer, H. S., Wimmer, V. C., Oberlaender, M., de Kock, C. P. J., Sakmann, B., & Helmstaedter, M. (2010). Number and Laminar Distribution of Neurons in a Thalamocortical Projection Column of Rat Vibrissal Cortex. *Cerebral Cortex, 20*(10), 2277–2286. https://doi.org/10.1093/cercor/bhq067

Morris, G., & Lecar, H. (1981). Voltage oscillations in the barnacle giant muscle fiber. *Biophysical Journal, 35*(1), 193–213.

Naud, R., & Gerstner, W. (2013). Can we predict every spike? In P. M. Dilorenzo & J. D. Victor (Eds.), *Spike Timing: Mechanisms and Function* (Issue November, pp. 65–76). CRC Press. http://www.amazon.com/Spike-Timing-Mechanisms-Frontiers-Neuroscience/dp/1439838151

Oberlaender, M., de Kock, C. P. J., Bruno, R. M., Ramirez, A., Meyer, H. S., Dercksen, V. J., Helmstaedter, M., & Sakmann, B. (2012). Cell Type-Specific Three-Dimensional Structure of Thalamocortical Circuits in a Column of Rat Vibrissal Cortex. *Cerebral Cortex, 22*(10), 2375–2391. https://doi.org/10.1093/cercor/bhr317

Oberlaender, M., Dercksen, V. J., Egger, R., Gensel, M., Sakmann, B., & Hege, H.-C. (2009). Automated three-dimensional detection and counting of neuron somata. *Journal of Neuroscience Methods, 180*(1), 147–160. https://doi.org/10.1016/j.jneumeth.2009.03.008

O'Connor, D. H., Huber, D., & Svoboda, K. (2009). Reverse engineering the mouse brain. *Nature, 461*(7266), 923–929. https://doi.org/10.1038/nature08539

O'Connor, D. H., Peron, S. P., Huber, D., & Svoboda, K. (2010). Neural Activity in Barrel Cortex Underlying Vibrissa-Based Object Localization in Mice. *Neuron, 67*(6), 1048–1061. https://doi.org/10.1016/j.neuron.2010.08.026

Otsu, N. (1979). A Threshold Selection Method from Gray-Level Histograms. *IEEE Transactions on Systems, Man, and Cybernetics, 9*(1), 62–66. https://doi.org/10.1109/TSMC.1979.4310076

Packer, A. M., & Yuste, R. (2011). Dense, Unspecific Connectivity of Neocortical Parvalbumin-Positive Interneurons: A Canonical Microcircuit for Inhibition? *The Journal of Neuroscience, 31*(37), 13260–13271. https://doi.org/10.1523/JNEUROSCI.3131-11.2011

Paninski, L. (2004). Maximum likelihood estimation of cascade point-process neural encoding models. *Network: Computation in Neural Systems*, *15*(4), 243–262. https://doi.org/10.1088/0954-898X/15/4/002

Peng, H., Ruan, Z., Long, F., Simpson, J. H., & Myers, E. W. (2010). V3D enables real-time 3D visualization and quantitative analysis of large-scale biological image data sets. *Nature Biotechnology, 28*(4), 348. https://doi.org/10.1038/nbt.1612

Peron, S. P., Freeman, J., Iyer, V., Guo, C., & Svoboda, K. (2015). A Cellular Resolution Map of Barrel Cortex Activity during Tactile Behavior. *Neuron, 86*(3), 783–799. https://doi.org/10.1016/j.neuron.2015.03.027

Peron, S. P., Pancholi, R., Voelcker, B., Wittenbach, J. D., Ólafsdóttir, H. F., Freeman, J., & Svoboda, K. (2020). Recurrent interactions in local cortical circuits. *Nature,* 1–4. https://doi.org/10.1038/s41586-020-2062-x

Petersen, C. C. H. (2007). The Functional Organization of the Barrel Cortex. *Neuron, 56*(2), 339–355. https://doi.org/10.1016/j.neuron.2007.09.017

Petersen, C. C. H., & Sakmann, B. (2001). Functionally Independent Columns of Rat Somatosensory Barrel Cortex Revealed with Voltage-Sensitive Dye Imaging. *Journal of Neuroscience, 21*(21), 8435–8446. https://doi.org/10.1523/JNEUROSCI.21-21-08435.2001

Petersen, R. S., Brambilla, M., Bale, M. R., Alenda, A., Panzeri, S., Montemurro, M. A., & Maravall, M. (2008). Diverse and temporally precise kinetic feature selectivity in the VPm thalamic nucleus. *Neuron*, *60*, 890–903. https://doi.org/10.1016/j.neuron.2008.09.041

Phoka, E., Wildie, M., Schultz, S. R., & Barahona, M. (2012). Sensory experience modifies spontaneous state dynamics in a large-scale barrel cortical model. *Journal of Computational Neuroscience, 33*(2), 323–339. https://doi.org/10.1007/s10827-012-0388-6

Pillow, J. W., Shlens, J., Paninski, L., Sher, A., Litke, A. M., Chichilnisky, E. J., & Simoncelli, E. P. (2008). Spatio-temporal correlations and visual signalling in a complete neuronal population. *Nature, 454*(7207), 995–999. https://doi.org/10.1038/nature07140

Porter, J. T., Cauli, B., Staiger, J. F., Lambolez, B., Rossier, J., & Audinat, E. (1998). Properties of bipolar VIPergic interneurons and their excitation by pyramidal neurons in the rat neocortex. *European Journal of Neuroscience, 10*(12), 3617–3628. https://doi.org/10.1046/j.1460-9568.1998.00367.x

Potjans, T. C., & Diesmann, M. (2014). The cell-type specific cortical microcircuit: Relating structure and activity in a full-scale spiking network model. *Cerebral Cortex, 24*(3), 785–806. https://doi.org/10.1093/cercor/bhs358

Prinz, A. A., Bucher, D., & Marder, E. (2004). Similar network activity from disparate circuit parameters. *Nature Neuroscience, 7*(12), 1345–1352. https://doi.org/10.1038/nn1352

Rauch, A., La Camera, G., Luscher, H.-R., Senn, W., & Fusi, S. (2003). Neocortical pyramidal cells respond as integrate-and-fire neurons to in vivo-like input currents. *Journal of Neurophysiology, 90*(3), 1598–1612. https://doi.org/10.1152/jn.00293.2003

Reich, D. S., Victor, J. D., & Knight, B. W. (1998). The power ratio and the interval map: Spiking models and extracellular recordings. *The Journal of Neuroscience, 18*(23), 10090–10104.

Reimann, M. W., Anastassiou, C. A., Perin, R., Hill, S. L., Markram, H., & Koch, C. (2013). A biophysically detailed model of neocortical local field potentials predicts the critical role of active membrane currents. *Neuron, 79*(2), 375–390. https://doi.org/10.1016/j.neuron.2013.05.023

Rosenblatt, F. (1958). The perceptron: A probabilistic model for information storage and organization in the brain. *Psychological Review, 65*, 386–408.

Rossant, C., Goodman, D. F. M., Fontaine, B., Platkiewicz, J., Magnusson, A. K., & Brette, R. (2011). Fitting neuron models to spike trains. *Frontiers in Neuroscience, 5*(February), 9. https://doi.org/10.3389/fnins.2011.00009

Rossant, C., Goodman, D. F. M., Platkiewicz, J., & Brette, R. (2010). Automatic fitting of spiking neuron models to electrophysiological recordings. *Frontiers in Neuroinformatics, 4*(2), 1–10. https://doi.org/10.3389/neuro.11.002.2010

Rubin, J., & Terman, D. (2004). High Frequency Stimulation of the Subthalamic Nucleus Eliminates Pathological Thalamic Rhythmicity in a Computational Model. *Journal of Computational Neuroscience, 16*, 211–235.

Schmidt, M., Bakker, R., Hilgetag, C. C., Diesmann, M., & van Albada, S. J. (2018a). Multi-scale account of the network structure of macaque visual cortex. *Brain Structure and Function, 223*(3), 1409–1435. https://doi.org/10.1007/s00429-017-1554-4

Schmidt, M., Bakker, R., Shen, K., Bezgin, G., Diesmann, M., & van Albada, S. J. (2018b). A multi-scale layer-resolved spiking network model of resting-state dynamics in macaque visual cortical areas. *PLOS Computational Biology, 14*(10), e1006359. https://doi.org/10.1371/journal.pcbi.1006359

Schuecker, J., Schmidt, M., van Albada, S. J., Diesmann, M., & Helias, M. (2017). Fundamental Activity Constraints Lead to Specific Interpretations of the Connectome. *PLOS Computational Biology, 13*(2), e1005179. https://doi.org/10.1371/journal.pcbi.1005179

Sermet, B. S., Truschow, P., Feyerabend, M., Mayrhofer, J. M., Oram, T. B., Yizhar, O., Staiger, J. F., & Petersen, C. C. (2019). Pathway-, layer- and cell-type-specific thalamic input to mouse barrel cortex. *eLife, 8*, e52665. https://doi.org/10.7554/eLife.52665

Seung, H. S., & Yuste, R. (2012). Neural Networks. In E. R. Kandel, J. H. Schwartz, T. M. Jessell, S. A. Siegelbaum, & A. J. Hudspeth (Eds.), *Principles of Neural Science* (5th ed., pp. 1581–1600). McGraw-Hill.

Sharp, T., Petersen, R., & Furber, S. (2014). Real-time million-synapse simulation of rat barrel cortex. *Frontiers in Neuroscience*, *8*(8 MAY), 1–9. https://doi.org/10.3389/fnins.2014.00131

Simons, D. J., & Carvell, G. E. (1989). Thalamocortical response transformation in the rat vibrissa/barrel system. *Journal of Neurophysiology, 61*(2), 311–330. https://doi.org/10.1152/jn.1989.61.2.311

Sompolinsky, H., Crisanti, A., & Sommers, H. J. (1988). Chaos in Random Neural Networks. *Physical Review Letters, 61*(3), 259–262.

Staiger, J. F., Flagmeyer, I., Schubert, D., Zilles, K., Kötter, R., & Luhmann, H. J. (2004). Functional Diversity of Layer IV Spiny Neurons in Rat Somatosensory Cortex: Quantitative Morphology of Electrophysiologically Characterized and Biocytin Labeled Cells. *Cerebral Cortex, 14*(6), 690–701. https://doi.org/10.1093/cercor/bhh029

Stam, C. J., & Reijneveld, J. C. (2007). Graph theoretical analysis of complex networks in the brain. *Nonlinear Biomedical Physics, 1*(1), 3. https://doi.org/10.1186/1753-4631-1-3

Stimberg, M., Brette, R., & Goodman, D. F. (2019). Brian 2, an intuitive and efficient neural simulator. *eLife, 8*, 1–41. https://doi.org/10.7554/elife.47314

Sudhakar, S. K., Hong, S., Raikov, I., Publio, R., Lang, C., Close, T., Guo, D., Negrello, M., & De Schutter, E. (2017). Spatiotemporal network coding of physiological mossy fiber inputs by the cerebellar granular layer. In *PLoS Computational Biology* (Vol. 13, Issue 9). https://doi.org/10.1371/journal.pcbi.1005754

Sun, Q.-Q., Huguenard, J. R., & Prince, D. A. (2006). Barrel Cortex Microcircuits: Thalamocortical Feedforward Inhibition in Spiny Stellate Cells Is Mediated by a Small Number of Fast-Spiking Interneurons. *Journal of Neuroscience, 26*(4), 1219–1230. https://doi.org/10.1523/JNEUROSCI.4727-04.2006

Swadlow, H. A. (1995). Influence of VPM afferents on putative inhibitory interneurons in S1 of the awake rabbit: Evidence from cross-correlation, microstimulation, and latencies to peripheral sensory stimulation. *Journal of Neurophysiology, 73*(4), 1584–1599. https://doi.org/10.1152/jn.1995.73.4.1584

Swadlow, H. A. (2003). Fast-spike Interneurons and Feedforward Inhibition in Awake Sensory Neocortex. *Cerebral Cortex, 13*(1), 25–32. https://doi.org/10.1093/cercor/13.1.25

Tamás, G., Andrea Lőrincz, A. S., & Szabadics, J. (2003). Identified Sources and Targets of Slow Inhibition in the Neocortex. *Science, 299*(5614), 1902–1905. https://doi.org/10.1126/science.1082053

Tamás, G., Buhl, E. H., Lörincz, A., & Somogyi, P. (2000). Proximally targeted GABAergic synapses and gap junctions synchronize cortical interneurons. *Nature Neuroscience, 3*(4), 366–371. https://doi.org/10.1038/73936

Thomson, A. M., & Lamy, C. (2007) Functional maps of neocortical local circuitry. *Frontiers in Neuroscience*, 1. https://doi.org/10.3389/neuro.01.1.1.002.2007

Tomsett, R. J., Ainsworth, M., Thiele, A., Sanayei, M., Chen, X., Gieselmann, M. A., Whittington, M. A., Cunningham, M. O., & Kaiser, M. (2015). Virtual Electrode Recording Tool for EXtracellular potentials (VERTEX): Comparing multi-electrode recordings from simulated and biological mammalian cortical tissue. *Brain Structure and Function, 220*(4), 2333–2353. https://doi.org/10.1007/s00429-014-0793-x

Tort, A. B., Rotstein, H. G., Dugladze, T., Gloveli, T., & Kopell, N. J. (2007). On the formation of gamma-coherent cell assemblies by oriens lacunosum-moleculare interneurons in the hippocampus. *Proceedings of the National Academy of Sciences, 104*(33), 13490–13495.

Traub, R. D., Contreras, D., Cunningham, M. O., Murray, H., LeBeau, F. E. N., Roopun, A., Bibbig, A., Bryan Wilent, W., Higley, M. J., Whittington, M., & a, Wilent, W. B., Higley, M. J., & Whittington, M. a. (2005). Single-Column Thalamocortical Network Model Exhibiting Gamma Oscillations, Sleep Spindles, and Epileptogenic Bursts. *Journal of Neurophysiology, 93*(4), 194–232. https://doi.org/10.1152/jn.00983.2004

Truccolo, W., Eden, U. T., Fellows, M. R., Donoghue, J. P., & Brown, E. N. (2005). A point process framework for relating neural spiking activity to spiking history, neural ensemble, and extrinsic covariate effects. *Journal of Neurophysiology, 93*(2), 1074–1089. https://doi.org/10.1152/jn.00697.2004

Tsai, P. S., Kaufhold, J. P., Blinder, P., Friedman, B., Drew, P. J., Karten, H. J., Lyden, P. D., & Kleinfeld, D. (2009). Correlations of Neuronal and Microvascular Densities in Murine Cortex Revealed by Direct Counting and Colocalization of Nuclei and Vessels. *Journal of Neuroscience, 29*(46), 14553–14570. https://doi.org/10.1523/JNEUROSCI.3287-09.2009

Uematsu, M., Hirai, Y., Karube, F., Ebihara, S., Kato, M., Abe, K., Obata, K., Yoshida, S., Hirabayashi, M., Yanagawa, Y., & Kawaguchi, Y. (2008). Quantitative Chemical Composition of Cortical GABAergic Neurons Revealed in Transgenic Venus-Expressing Rats. *Cerebral Cortex, 18*(2), 315–330. https://doi.org/10.1093/cercor/bhm056

van Vreeswijk, C., & Sompolinsky, H. (1996). Chaos in neuronal networks with balanced excitatory and inhibitory activity. *Science, 274*, 1724–1726.

van Vreeswijk, C., & Sompolinsky, H. (1998). Chaotic Balanced State in a Model Of Cortical Circuits. *Neural Computation, 10*, 1321–1371.

Varshney, L. R., & Chen, B. L. (2011). Structural Properties of the Caenorhabditis elegans Neuronal Network. *PLoS Computational Biology, 12596*(2), 1–41. https://doi.org/10.1371/journal.pcbi.1001066

Vincent, L. (1993). Morphological grayscale reconstruction in image analysis: Applications and efficient algorithms. *IEEE Transactions on Image Processing, 2*(2), 176–201. https://doi.org/10.1109/83.217222

Vogelstein, J. T., Watson, B. O., Packer, A. M., Yuste, R., Jedynak, B., & Paninski, L. (2009). Spike inference from calcium imaging using sequential Monte Carlo methods. *Biophysical Journal, 97*(2), 636–655. https://doi.org/10.1016/j.bpj.2008.08.005

Wang, Y., Toledo-Rodriguez, M., Gupta, A., Wu, C., Silberberg, G., Luo, J., & Markram, H. (2004). Anatomical, physiological and molecular properties of Martinotti cells in the somatosensory cortex of the juvenile rat. *The Journal of Physiology, 561*(1), 65–90. https://doi.org/10.1113/jphysiol.2004.073353

Watts, D. J., & Strogatz, S. H. (1998). Collective dynamics of "small-world" networks. *Nature, 393*(6684), 440–442.

Wendling, F., Bartolomei, F., Bellanger, J. J., & Chauvel, P. (2002). Epileptic fast activity can be explained by a model of impaired GABAergic dendritic inhibition. *European Journal of Neuroscience, 15*, 1499–1508.

White, E. L. (1979). Thalamocortical synaptic relations: A review with emphasis on the projections of specific thalamic nuclei to the primary sensory areas of the neocortex. *Brain Research Reviews, 1*(3), 275–311. https://doi.org/10.1016/0165-0173(79)90008-0

Woo, J., Kim, S. H., Han, K., & Choi, M. (2021). Characterization of dynamics and information processing of integrate-and-fire neuron models. *Journal of Physics a: Mathematical and Theoretical, 54*(44), 445601. https://doi.org/10.1088/1751-8121/ac2a54

Wozny, C., & Williams, S. R. (2011). Specificity of Synaptic Connectivity between Layer 1 Inhibitory Interneurons and Layer 2/3 Pyramidal Neurons in the Rat Neocortex. *Cerebral Cortex, 21*(8), 1818–1826. https://doi.org/10.1093/cercor/bhq257

Xu, X., Roby, K. D., & Callaway, E. M. (2006). Mouse cortical inhibitory neuron type that coexpresses somatostatin and calretinin. *Journal of Comparative Neurology, 499*(1), 144–160. https://doi.org/10.1002/cne.21101

Zeldenrust, F., Calcini, N., Yan, X., Bijlsma, A., & Celikel, T. (2020). Cell type specific information transfer for sparse coding. *BioRxiv*, 2020.11.06.371658. https://doi.org/10.1101/2020.11.06.371658

Zeldenrust, F., Wadman, W. J., & Englitz, B. (2018). Neural Coding With Bursts-Current State and Future Perspectives. *Frontiers in Computational Neuroscience, 12*(48), 1–14. https://doi.org/10.3389/fncom.2018.00048.

Zheng, Y., Lin, S., Kambhamettu, C., Yu, J., & Kang, S. B. (2009). Single-Image Vignetting Correction. *IEEE Transactions on Pattern Analysis and Machine Intelligence, 31*(12), 2243–2256. https://doi.org/10.1109/TPAMI.2008.263

Zhu, W., Shelley, M., & Shapley, R. (2009). A neuronal network model of primary visual cortex explains spatial frequency selectivity. *Journal of Computational Neuroscience, 26*(2), 271–287. https://doi.org/10.1007/s10827-008-0110-x